

# Runge-Kutta discontinuous local evolution Galerkin methods for the shallow water equations on the cubed-sphere

Yangyu Kuang, Kailiang Wu, Huazhong Tang<sup>1</sup>

*HEDPS, CAPT & LMAM, School of Mathematical Sciences, Peking University,  
Beijing 100871, P.R. China*

---

## Abstract

The paper develops high order accurate Runge-Kutta discontinuous local evolution Galerkin (RKDLEG) methods on the cubed-sphere grid for the shallow water equations (SWEs). Instead of using the dimensional splitting method or solving one-dimensional Riemann problem in the direction normal to the cell interface, the RKDLEG methods are built on genuinely multi-dimensional approximate local evolution operator of the locally linearized SWEs on a sphere by considering all bicharacteristic directions. Several numerical experiments are conducted to demonstrate the accuracy and performance of our RKDLEG methods, in comparison to the Runge-Kutta discontinuous Galerkin method with Godunov's flux etc.

*Key words:* RKDLEG method, evolution operator, genuinely multi-dimensional method, shallow water equations, cubed-sphere grid.

---

## 1 Introduction

The shallow water equations (SWEs) describe the motion of a thin layer of fluid held down by gravity. The SWEs on the sphere exhibit the major difficulties associated with the horizontal dynamical aspects of atmospheric modeling on the spherical earth and thus are important in studying the dynamics of large-scale atmospheric flows and developing numerical methods of more complex atmospheric models. In comparison with the planar case, the main difficulties in solving the SWEs on the sphere come from the spherical geometry, the choice of coordinates, nonlinearity, and the large scale difference between

---

*Email addresses:* [kyy@pku.edu.cn](mailto:kyy@pku.edu.cn) (Yangyu Kuang), [wuk1@pku.edu.cn](mailto:wuk1@pku.edu.cn) (Kailiang Wu), [hztang@math.pku.edu.cn](mailto:hztang@math.pku.edu.cn) (Huazhong Tang).

<sup>1</sup> Corresponding author. Tel: +86-10-62757018; Fax: +86-10-62751801.

the horizontal and vertical motions of the fluids. High-order accurate numerical methods are becoming increasingly popular in atmospheric modeling, but the numerical methods should be competent for long time simulation. In order to evaluate numerical methods for the solutions of SWEs in spherical geometry, Williamson et al. proposed a suite of seven test cases and offered reference solutions to those tests obtained by using a pseudo-spectral method [49].

Representation of the spherical geometry plays an important role in solving SWEs on the sphere. The latitude-longitude (LAT/LON) coordinates or grids are naturally and popularly chosen in the early stage [2,24,31], but the singularity at the poles leads to big numerical difficulty. Overcoming such pole singularity needs special numerical technique and boundary conditions [39]. To avoid the pole singularity in the LAT/LON coordinates, other choices are the icosahedral hexagonal or triangular grids [19,21,36,47], Yin-Yang grid [18,22,23], and cubed-sphere grid [7,34,37,38,39,48]. Comparisons of those frequently-used grids are given in [6,41]. An icosahedral-hexagonal grid on the sphere is created by dividing the faces of an icosahedron and projecting the vertices onto the sphere, thus it is non-quadrilateral and unstructured. The Yin-Yang grid is overset in spherical geometry and composes of two identical component grids combined in a complementary way to cover a spherical surface with partial overlap on their boundaries so that the interpolation should be used between two component grids. The cubed-sphere grid is quasi-uniform and easily generated by dividing the sphere into six identical regions with the aid of projection of the sides of a circumscribed cube onto a spherical surface and choosing the coordinate lines on each region to be arcs of great circles. The mainly existing numerical methods for the SWEs on the sphere are as follows: finite-difference [2,39,46,47], finite-volume [21,24,51], multi-moment finite volume [6,7,22,23], spectral transform [16], spectral element [12,43,45], and discontinuous Galerkin (DG) methods [11,13,19,34,35] etc. Most of them are built on the one-dimensional exact or approximate Riemann solver.

The aim of the paper is to develop Runge-Kutta discontinuous local evolution Galerkin (RKDLEG) methods for the SWEs on the cubed sphere. They are the (genuinely) multi-dimensional and combining the Runge-Kutta discontinuous Galerkin (RKDG) methods on the cubed-sphere with the local evolution Galerkin (LEG) method, which is a modification and simplification of the original finite volume evolution Galerkin (EG) method for multi-dimensional nonlinear hyperbolic system [30,42]. The EG method generalizes the Godunov method by using an evolution operator coupling the flux formulation of each direction for the multi-dimensional hyperbolic system. The basic idea of the EG method was introduced in [32], and then it was developed for the linear hyperbolic system in [27] and nonlinear hyperbolic systems in [26,30]. The EG method is constructed by using the theory of bicharacteristics in order to take all infinitely many directions of wave propagation into account and give the exact and approximate evolution operators of the linearized hyperbolic system, in other words, integrating the linearized hyperbolic system along its bicharacteristics to obtain an equivalent integral system, then making a suitable approximations of the integral system. Similar bicharacteristic-type methods for hyperbolic system, can be found in the early literature such as [5,14,17]. The EG method may be considered as a genuinely multi-dimensional Godunov-type scheme, in which the

so-called approximate evolution operator is used to get the explicit approximate solutions at each cell interface along all infinite bicharacteristics of the linearized system, instead of solving the local one-dimensional Riemann problem in direction normal to each cell interface by any Riemann solver. It has been used successfully for various physical applications, e.g. the wave propagation in heterogeneous media [1], the Euler equations of gas dynamics [28], and the SWEs [4,9,15,29] with well-balanced property with or without dry beds. A survey of finite volume EG method was presented in [25]. The LEG method was proposed in [42] to simplify the evaluation of the EG numerical fluxes by taking the limit of the approximate evolution operator at time level  $t_n$  as the time  $t_n + \tau$  approaches  $t_n$ . It has been successfully extended to the relativistic hydrodynamics [50]. Few attentions were paid to a combination of the RKDG methods with the EG operator for the highly accurate simulation of planar compressible flows, see e.g. [3,52]. It is challenging to extend the EG or LEG method to the SWEs in the spherical geometry. Due to the complex geometry and the choice of coordinates, the derivation of evolution operator is much more complicate than the planar case.

The paper is organized as follows. Section 2 introduces the cubed-sphere grid and spherical SWEs and derives the exact evolution operator of the locally linearized spherical SWEs in the reference coordinates. Section 3 presents our RKDLEG method in the reference coordinates, including the DG spatial discretization in Section 3.1, Runge-Kutta time discretization in Section 3.2, and the approximate evolution operators in the cubed sphere face in Section 3.3, where a special treatment is given for the points on the edges of cubed sphere face in order to preserve the conservation of numerical fluxes there. The approximate local evolution operator is equal to the limit of the approximate evolution operator as the time parameter tends to zero, Section 4 conducts several numerical experiments to demonstrate the accuracy and effectiveness as well as the multi-dimensional behavior of the proposed RKDLEG method. Section 5 concludes the paper.

## 2 Preliminaries and notations

This section introduces the cubed-sphere grid and SWEs, and derives the exact evolution operator of the locally linearized SWEs in spherical geometry.

### 2.1 The cubed-sphere grid

Since the cubed-sphere grid was proposed, it has widely been used in the literature because the boundary conditions at the pole in spherical coordinates are seen to vanish in the finite-difference formulation [39]. It was numerically demonstrated that the cubed-sphere grid with gnomonic (equiangular central) projection was an excellent choice for high-order accurate numerical methods in global modeling applications, see e.g. [34,35] etc.

The sphere with radius of  $R$  is decomposed into 6 identical cubed-sphere faces  $\{P_i, i =$

$1, 2, \dots, 6\}$  by using the central (gnomonic) projection of an inscribed cube with side  $\frac{2\sqrt{3}}{3}R$  [39], see Fig. 2.1 (a), where the thick line denotes the edge of cubed-sphere face. There are two different central projections: employing the local Cartesian coordinates [39] and the equiangular (central) coordinates [38,44]. In the equiangular projection, each face of cube or cubed-sphere may be mapped to a reference region  $\tilde{\Omega} = [-\frac{\pi}{4}, \frac{\pi}{4}] \times [-\frac{\pi}{4}, \frac{\pi}{4}]$ , in which the equiangular (central) coordinates are denoted by  $x$  and  $y$  here. As an example, the mapping relation between the cubed-sphere face  $P_1$  and the reference region  $\tilde{\Omega}$  is given by

$$x = \xi, \quad y = \arctan\left(\frac{\tan \eta}{\cos \xi}\right), \quad (2.1)$$

where  $\eta \in [-\arctan(|\cos \xi|), \arctan(|\cos \xi|)] \subset [-\frac{\pi}{2}, \frac{\pi}{2}]$ ,  $\xi \in [-\frac{\pi}{4}, \frac{\pi}{4}] \subset [-\pi, \pi)$ , and  $\xi$  and  $\eta$  denote the longitude and latitude (LAT/LON) coordinates. In fact, the transformation rules in (2.1) are also satisfied for any face of the cubed-sphere in rotated LAT/LON coordinates  $(\xi, \eta)$  with the origin located at the center of corresponding face. With the application of the transformations between the rotated and original LAT/LON coordinates, the transformation rules for other faces of the cubed-sphere can be obtained, see Appendix A of [34] for a detailed description.

Divide  $\tilde{\Omega}$  into a square grid, see Fig. 2.1 (b), and then such grid is inversely mapped to the cubed-sphere face to get the cubed-sphere grid, see its schematic diagram in Fig. 2.1 (c). It is worth noting that the equiangular projection generates more uniform grid on the sphere as opposed to the equidistant projection [34], the reference coordinate system is free of pole singularities, and all grid lines on the sphere are great-circle arcs. However, the transformation from  $\tilde{\Omega}$  to the sphere is not conformal and such central mapping creates identical non-orthogonal curvilinear coordinates on each face of the cubed-sphere.

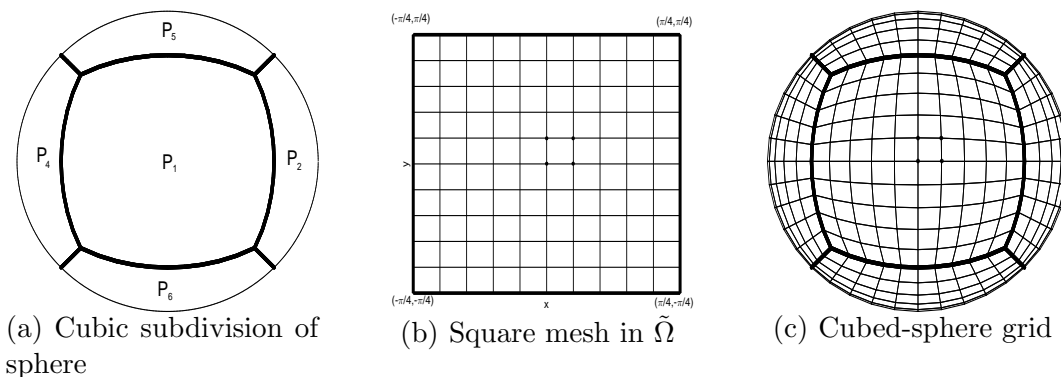


Fig. 2.1. Schematic diagram of the cubed-sphere and cubed-sphere grid.

It is now possible to compute the metric tensor and corresponding quantities using (2.1). Let  $\mathbf{r}$  be the position vector of the point on the spherical surface, and  $\mathbf{v}$  denote the velocity vector of the fluid on the sphere satisfying  $\mathbf{v} \cdot \mathbf{k} = 0$ , where  $\mathbf{k}$  is the outward unit normal vector of the spherical surface. The covariant velocity  $(\hat{u}, \hat{v})$  may be calculated by  $\hat{u} = \mathbf{v} \cdot \frac{\partial \mathbf{r}}{\partial x}$ ,  $\hat{v} = \mathbf{v} \cdot \frac{\partial \mathbf{r}}{\partial y}$ , while the contravariant velocity  $(u, v)$  may be given by solving  $\mathbf{v} = u \frac{\partial \mathbf{r}}{\partial x} + v \frac{\partial \mathbf{r}}{\partial y}$  and  $\mathbf{v} \cdot \mathbf{k} = 0$ , where  $\frac{\partial \mathbf{r}}{\partial x}$  and  $\frac{\partial \mathbf{r}}{\partial y}$  denote the covariant base vectors of the transformation between the reference region  $\tilde{\Omega}$  and spherical surface. If using  $(u_s, v_s)$  to



denote the velocity in LAT/LON coordinates  $(\xi, \eta)$ , that is,  $u_s$  and  $v_s$  are the longitude and latitude components of the velocity respectively, then the relations among  $(u_s, v_s)$ ,  $(u, v)$  and  $(\hat{u}, \hat{v})$  can be given by

$$\mathbf{A} \begin{pmatrix} u \\ v \end{pmatrix} = \begin{pmatrix} u_s \\ v_s \end{pmatrix}, \quad \mathbf{A}^T \begin{pmatrix} u_s \\ v_s \end{pmatrix} = \begin{pmatrix} \hat{u} \\ \hat{v} \end{pmatrix}, \quad \mathbf{A} = \begin{pmatrix} R\xi_x \cos \eta & R\xi_y \cos \eta \\ R\eta_x & R\eta_y \end{pmatrix}, \quad (2.2)$$

where  $R$  is the radius of the sphere. The metric tensor  $\mathbf{G}$  for the above transformation can be obtained by

$$\mathbf{G} = \begin{pmatrix} g_{11} & g_{12} \\ g_{21} & g_{22} \end{pmatrix} = \mathbf{A}^T \mathbf{A} = \frac{R^2}{\rho^4 \cos^2 x \cos^2 y} \begin{pmatrix} 1 + \tan^2 x & -\tan x \tan y \\ -\tan x \tan y & 1 + \tan^2 y \end{pmatrix}, \quad (2.3)$$

and its inverse is

$$\mathbf{G}^{-1} = \begin{pmatrix} g^{11} & g^{12} \\ g^{21} & g^{22} \end{pmatrix} = \frac{1}{\det(\mathbf{G})} \begin{pmatrix} g_{22} & -g_{12} \\ -g_{21} & g_{11} \end{pmatrix}, \quad (2.4)$$

where  $\rho^2 = 1 + \tan^2 x + \tan^2 y$ . It is worth noting that the metric tensor has the same form for each face of the cubed-sphere [35], and some special numerical treatments are required around the edges of the cubed-sphere face, see Section 3, because the coordinate transformation across the edges of the cubed-sphere face is not continuous.

## 2.2 Governing equations

The spherical shallow water equations in the LAT/LON coordinates  $(\xi, \eta)$  may be written as follows [49]

$$\begin{aligned} \frac{\partial h}{\partial t} + \frac{1}{R \cos \eta} \left[ \frac{\partial}{\partial \xi} (h u_s) + \frac{\partial}{\partial \eta} (h v_s \cos \eta) \right] &= 0, \\ \frac{\partial u_s}{\partial t} + \frac{1}{R \cos \eta} \left[ \frac{\partial (g(h+b))}{\partial \xi} + \left( u_s \frac{\partial u_s}{\partial \xi} + v_s \cos \eta \frac{\partial u_s}{\partial \eta} \right) \right] - f v_s - \frac{u_s \tan \eta}{R} v_s &= 0, \\ \frac{\partial v_s}{\partial t} + \frac{1}{R \cos \eta} \left[ \cos \eta \frac{\partial (g(h+b))}{\partial \eta} + \left( u_s \frac{\partial v_s}{\partial \xi} + v_s \cos \eta \frac{\partial v_s}{\partial \eta} \right) \right] + f u_s + \frac{u_s \tan \eta}{R} u_s &= 0, \end{aligned} \quad (2.5)$$

where  $b$  denotes the height of the bottom mountain,  $h$  is the height of the fluid over the bottom mountain,  $u_s$  and  $v_s$  are two velocity components in the longitude  $\xi$  and latitude  $\eta$  directions respectively,  $g$  is the gravitational constant,  $f$  is the Coriolis parameter defined by  $f = 2\Omega \sin \theta$ , and  $\Omega = 7.292 \times 10^{-5} \text{ s}^{-1}$  is the angular speed of the Earth's rotation.

Under the transformation between the LAT/LON coordinates  $(\xi, \eta)$  and the reference coordinates  $(x, y)$ , given in Section 2.1, the SWEs (2.5) may be transformed into the

following divergence form [51]

$$\frac{\partial \mathbf{U}}{\partial t} + \frac{\partial \mathbf{F}_1}{\partial x} + \frac{\partial \mathbf{F}_2}{\partial y} = \mathbf{S}_0, \quad (2.6)$$

where

$$\mathbf{U} = \begin{pmatrix} \Lambda h \\ \Lambda hu \\ \Lambda hv \end{pmatrix}, \quad \mathbf{F}_1 = \begin{pmatrix} \Lambda hu \\ \Lambda \left( hu^2 + \frac{1}{2} gg^{11} h^2 \right) \\ \Lambda \left( huv + \frac{1}{2} gg^{12} h^2 \right) \end{pmatrix}, \quad \mathbf{F}_2 = \begin{pmatrix} \Lambda hv \\ \Lambda \left( huv + \frac{1}{2} gg^{12} h^2 \right) \\ \Lambda \left( hv^2 + \frac{1}{2} gg^{22} h^2 \right) \end{pmatrix}, \quad \mathbf{S}_0 = \begin{pmatrix} 0 \\ \Lambda S_0^{(1)} \\ \Lambda S_0^{(2)} \end{pmatrix},$$

Here  $(u, v)$  denotes the contravariant velocity vector,  $\Lambda = \sqrt{\det(\mathbf{G})}$  is the Jacobian of the transformation,  $\mathbf{G}$  is defined in (2.3), and

$$\begin{aligned} S_0^{(1)} &= -\Gamma_{11}^1 hu^2 - 2\Gamma_{12}^1 huv - f\Lambda \left( g^{12} hu - g^{11} hv \right) - gh \left( g^{11} b_x + g^{12} b_y \right), \\ S_0^{(2)} &= -\Gamma_{22}^2 hv^2 - 2\Gamma_{12}^2 huv - f\Lambda \left( g^{22} hu - g^{12} hv \right) - gh \left( g^{12} b_x + g^{22} b_y \right), \end{aligned}$$

in which the Christoffel symbols are given by [51]

$$\Gamma_{11}^1 = \frac{2 \tan x \tan^2 y}{\rho^2}, \quad \Gamma_{12}^1 = -\frac{\tan y}{\rho^2 \cos^2 y}, \quad \Gamma_{12}^2 = -\frac{\tan x}{\rho^2 \cos^2 x}, \quad \Gamma_{22}^2 = \frac{2 \tan^2 x \tan y}{\rho^2}.$$

When the solutions are smooth, (2.6) is equivalent to the following primitive variable form

$$\frac{\partial \mathbf{V}}{\partial t} + \mathbf{A}_1(\mathbf{V}, \mathbf{x}) \frac{\partial \mathbf{V}}{\partial x} + \mathbf{A}_2(\mathbf{V}, \mathbf{x}) \frac{\partial \mathbf{V}}{\partial y} = \mathbf{S}_1, \quad (2.7)$$

where  $\mathbf{V} = (h, u, v)^T$ ,  $\mathbf{x} = (x, y)$ , and

$$\mathbf{A}_1(\mathbf{V}, \mathbf{x}) = \begin{pmatrix} u & h & 0 \\ gg^{11} & u & 0 \\ gg^{12} & 0 & u \end{pmatrix}, \quad \mathbf{A}_2(\mathbf{V}, \mathbf{x}) = \begin{pmatrix} v & 0 & h \\ gg^{12} & v & 0 \\ gg^{22} & 0 & v \end{pmatrix}.$$

Here the source term  $\mathbf{S}_1 = \mathbf{S}_1^B - \mathbf{S}_1^S$  with  $\mathbf{S}_1^B := (0, S_1^{B(1)}, S_1^{B(2)})^T$  and  $\mathbf{S}_1^S := (0, S_1^{S(1)}, S_1^{S(2)})^T$ , in which

$$\begin{aligned} S_1^{B(1)} &= g \left( g^{11} \frac{\partial b}{\partial x} + g^{12} \frac{\partial b}{\partial y} \right), \quad S_1^{B(2)} = g \left( g^{12} \frac{\partial b}{\partial x} + g^{22} \frac{\partial b}{\partial y} \right), \\ S_1^{S(1)} &= \Gamma_{11}^1 u^2 + 2\Gamma_{12}^1 uv + f\Lambda \left( g^{12} u - g^{11} v \right) \\ &\quad + \frac{1}{2} gh \left( \frac{\partial g^{11}}{\partial x} + \frac{\partial g^{12}}{\partial y} \right) + \frac{1}{2\Lambda} gh \left( \Lambda_x g^{11} + \Lambda_y g^{12} \right), \\ S_1^{S(2)} &= \Gamma_{22}^2 v^2 + 2\Gamma_{12}^2 uv - f\Lambda \left( g^{22} u - g^{12} v \right) \end{aligned}$$

$$+ \frac{1}{2}gh \left( \frac{\partial g^{12}}{\partial x} + \frac{\partial g^{22}}{\partial y} \right) + \frac{1}{2\Lambda}gh \left( \Lambda_x g^{12} + \Lambda_y g^{22} \right).$$

The system (2.7) or (2.6) is hyperbolic in time, and the linearized version of (2.7) becomes the start point of the approximate local evolution operator in our RKDLEG methods for the SWEs (2.6), see Section 2.3.

**Lemma 2.1 (Hyperbolicity in time)** *For all admissible states  $\mathbf{V}$  and any real angle  $\theta$ , the matrix  $\mathbf{A}(\mathbf{V}, \mathbf{x}; \theta) := \mathbf{A}_1(\mathbf{V}, \mathbf{x}) \cos \theta + \mathbf{A}_2(\mathbf{V}, \mathbf{x}) \sin \theta$  may be diagonalized as*

$$\mathbf{A}(\mathbf{V}, \mathbf{x}; \theta) = \mathbf{R}(\mathbf{V}, \mathbf{x}; \theta) \mathbf{\Lambda}(\mathbf{V}, \mathbf{x}; \theta) \mathbf{L}(\mathbf{V}, \mathbf{x}; \theta),$$

where  $\mathbf{\Lambda}(\mathbf{V}, \mathbf{x}; \theta)$  is a diagonal matrix with three real entries

$$\lambda^{(1)}(\mathbf{V}, \mathbf{x}; \theta) = v_\theta - cK_\theta, \quad \lambda^{(2)}(\mathbf{V}, \mathbf{x}; \theta) = v_\theta, \quad \lambda^{(3)}(\mathbf{V}, \mathbf{x}; \theta) = v_\theta + cK_\theta, \quad (2.8)$$

and the matrix  $\mathbf{L}(\mathbf{V}, \mathbf{x}; \theta)$  and its inverse  $\mathbf{R}(\mathbf{V}, \mathbf{x}; \theta)$  are given by

$$\mathbf{L}(\mathbf{V}, \mathbf{x}; \theta) = \begin{pmatrix} -\frac{1}{2} & \frac{c \cos \theta}{2gK_\theta} & \frac{c \sin \theta}{2gK_\theta} \\ 0 & \frac{G_s(\theta)}{K_\theta} & -\frac{G_c(\theta)}{K_\theta} \\ \frac{1}{2} & \frac{c \cos \theta}{2gK_\theta} & \frac{c \sin \theta}{2gK_\theta} \end{pmatrix}, \quad \mathbf{R}(\mathbf{V}, \mathbf{x}; \theta) = \begin{pmatrix} -1 & 0 & 1 \\ \frac{g}{c}G_c(\theta) & \sin \theta & \frac{g}{c}G_c(\theta) \\ \frac{g}{c}G_s(\theta) & -\cos \theta & \frac{g}{c}G_s(\theta) \end{pmatrix}. \quad (2.9)$$

Here

$$K_\theta = \sqrt{g^{11} \cos^2 \theta + g^{12} \sin 2\theta + g^{22} \sin^2 \theta}, \quad v_\theta = u \cos \theta + v \sin \theta, \quad c = \sqrt{gh}, \quad (2.10)$$

and

$$G_c(\theta) = \frac{g^{11} \cos \theta + g^{12} \sin \theta}{K_\theta}, \quad G_s(\theta) = \frac{g^{12} \cos \theta + g^{22} \sin \theta}{K_\theta}.$$

The proof of this lemma is trivial and omitted here.

### 2.3 Exact evolution operator

This section derives the exact evolution operator of the locally linearized SWEs, or equivalently, integrates the locally linearized SWEs along their bicharacteristics to give an equivalent integral system.

Use  $\tilde{\mathbf{x}} = (\tilde{x}, \tilde{y})$  and  $\tilde{\mathbf{V}} = (\tilde{h}, \tilde{u}, \tilde{v})^T$  to denote the reference position and state of the vector  $\mathbf{V}$  in (2.7), and linearize the system (2.7) as follows

$$\frac{\partial \mathbf{V}}{\partial t} + \mathbf{A}_1(\tilde{\mathbf{V}}, \tilde{\mathbf{x}}) \frac{\partial \mathbf{V}}{\partial x} + \mathbf{A}_2(\tilde{\mathbf{V}}, \tilde{\mathbf{x}}) \frac{\partial \mathbf{V}}{\partial y} = \mathbf{S}_1(\mathbf{V}, \mathbf{x}). \quad (2.11)$$

It is obvious that (2.11) is still hyperbolic in time thanks to Lemma 2.1. For the sake of convenience, we will shorten notations in the following such as  $\tilde{\mathbf{A}}_i := \mathbf{A}_i(\tilde{\mathbf{V}}, \tilde{\mathbf{x}})$ ,  $\tilde{\mathbf{L}}(\theta) := \mathbf{L}(\tilde{\mathbf{V}}, \tilde{\mathbf{x}}; \theta)$ ,  $\tilde{\mathbf{R}}(\theta) := \mathbf{R}(\tilde{\mathbf{V}}, \tilde{\mathbf{x}}; \theta)$ ,  $\tilde{\lambda}^{(\ell)}(\theta) := \lambda^{(\ell)}(\tilde{\mathbf{V}}, \tilde{\mathbf{x}}; \theta)$ , and so on.

Multiplying the system (2.11) from the left by  $\tilde{\mathbf{L}}(\theta)$  gives its characteristic form

$$\frac{\partial \mathbf{W}}{\partial t} + \tilde{\mathbf{B}}_1(\theta) \frac{\partial \mathbf{W}}{\partial x} + \tilde{\mathbf{B}}_2(\theta) \frac{\partial \mathbf{W}}{\partial y} = \tilde{\mathbf{L}}(\theta) \mathbf{S}_1, \quad (2.12)$$

or the quasi-diagonalized form

$$\frac{\partial \mathbf{W}}{\partial t} + \tilde{\mathbf{D}}_1(\theta) \frac{\partial \mathbf{W}}{\partial x} + \tilde{\mathbf{D}}_2(\theta) \frac{\partial \mathbf{W}}{\partial y} = \mathbf{S}(\mathbf{W}; \theta) + \mathbf{S}^{(a)}, \quad (2.13)$$

where  $\mathbf{W} = \tilde{\mathbf{L}}(\theta) \mathbf{V}$  is the characteristic variable vector with three components

$$w_1 = -\frac{h}{2} + \frac{\tilde{c}}{2g\tilde{K}_\theta} v_\theta, \quad w_2 = \frac{1}{\tilde{K}_\theta} [\tilde{G}_s(\theta)u - \tilde{G}_c(\theta)v], \quad w_3 = \frac{h}{2} + \frac{\tilde{c}}{2g\tilde{K}_\theta} v_\theta, \quad (2.14)$$

and the matrix  $\tilde{\mathbf{D}}_i(\theta)$  denotes the diagonal component of  $\tilde{\mathbf{B}}_i(\theta) = \tilde{\mathbf{L}}(\theta) \tilde{\mathbf{A}}_i \tilde{\mathbf{R}}(\theta)$ ,  $i = 1, 2$ . Moreover, the ‘‘source’’ terms are expressed by

$$\mathbf{S}(\mathbf{W}; \theta) := \left( \tilde{\mathbf{D}}_1(\theta) - \tilde{\mathbf{B}}_1(\theta) \right) \frac{\partial \mathbf{W}}{\partial x} + \left( \tilde{\mathbf{D}}_2(\theta) - \tilde{\mathbf{B}}_2(\theta) \right) \frac{\partial \mathbf{W}}{\partial y}, \quad (2.15)$$

and

$$\mathbf{S}^{(a)} = \tilde{\mathbf{L}}(\theta) \mathbf{S}_1.$$

Because the entry in the  $i$ th row and  $j$ th column of a matrix  $\tilde{\mathbf{B}}_i(\theta)$  is  $\tilde{\mathbf{L}}^{(i)}(\theta) \tilde{\mathbf{A}}_i \tilde{\mathbf{R}}^{(j)}(\theta)$ , where  $\tilde{\mathbf{L}}^{(i)}(\theta)$  denotes the  $i$ th row vector of the matrix  $\tilde{\mathbf{L}}(\theta)$  and  $\tilde{\mathbf{R}}^{(j)}(\theta)$  denotes the  $j$ th column vector of the matrix  $\tilde{\mathbf{R}}(\theta)$ , the diagonal entries of  $\tilde{\mathbf{D}}_i(\theta) = \text{diag} \{d_i^{(1)}(\theta), d_i^{(2)}(\theta), d_i^{(3)}(\theta)\}$  may be expressed as

$$d_i^{(\ell)}(\theta) = \tilde{\mathbf{L}}^{(\ell)}(\theta) \tilde{\mathbf{A}}_i \tilde{\mathbf{R}}^{(\ell)}(\theta), \quad \ell = 1, 2, 3, \quad i = 1, 2.$$

Those diagonal entries determine the bicharacteristics of (2.11) by

$$\frac{dx}{dt} = d_1^{(\ell)}(\theta), \quad \frac{dy}{dt} = d_2^{(\ell)}(\theta), \quad \ell = 1, 2, 3. \quad (2.16)$$

It is worth nothing that the second bicharacteristic direction does not depend on the real angle  $\theta$ . The left figure in Fig. 2.2 shows three bicharacteristics in the  $(x, y, t)$  space for a fixed angle  $\theta$ , i.e. straight (solid) line segments  $\text{PQ}_\ell$ ,  $\ell = 1, 2, 3$ , where  $\text{PQ}_2$  is also denoted by  $\text{PP}'$ , and the dotted line  $\text{PP}_0$  is only a line segment perpendicular to the horizontal  $(x, y)$  plane. If assuming that the coordinate of the point P is  $(x, y, t + \tau)$ , then ones of  $\text{P}_0$  and  $\text{Q}_\ell(\theta)$  are  $(x, y, t)$  and  $(x - d_1^{(\ell)}(\theta)\tau, y - d_2^{(\ell)}(\theta)\tau, t)$ , respectively,  $\ell = 1, 2, 3$ . The right plot in Fig. 2.2 displays corresponding bicharacteristic cone past the point P, which may be described by the set

$$\left\{ \left( x - d_1^{(\ell)}(\theta)\zeta, y - d_2^{(\ell)}(\theta)\zeta, t + \tau - \zeta \right), \quad \ell = 1, 3, \quad \theta \in [0, 2\pi), \quad \zeta \in [0, \tau] \right\}, \quad (2.17)$$

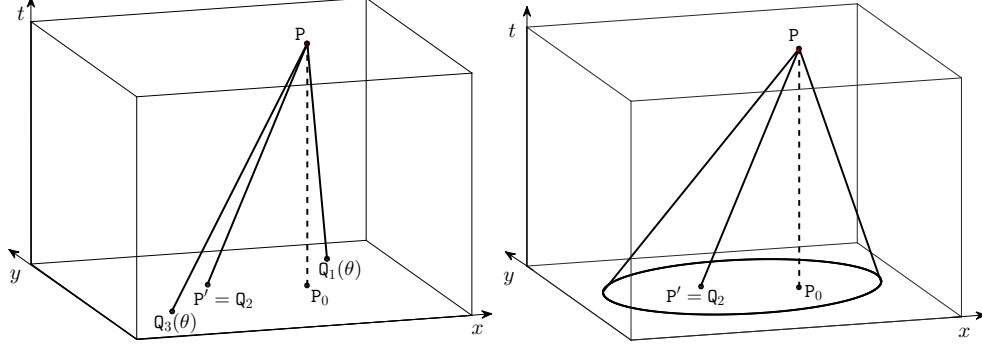


Fig. 2.2. The bicharacteristic curves with the fixed angle  $\theta$  (left) and the bicharacteristic cone (right) of the system (2.11).

which is an elliptic cone in general.

**Lemma 2.2** *The diagonal entries  $d_i^{(\ell)}(\theta)$  and the “source” term  $\mathbf{S}(\mathbf{W}; \theta)$  in the quasi-diagonalized system (2.13) have the following explicit form*

$$d_1^{(1)}(\theta) = \tilde{u} - \tilde{c}\tilde{G}_c(\theta), \quad d_1^{(2)}(\theta) = \tilde{u}, \quad d_1^{(3)}(\theta) = \tilde{u} + \tilde{c}\tilde{G}_c(\theta),$$

$$d_2^{(1)}(\theta) = \tilde{v} - \tilde{c}\tilde{G}_s(\theta), \quad d_2^{(2)}(\theta) = \tilde{v}, \quad d_2^{(3)}(\theta) = \tilde{v} + \tilde{c}\tilde{G}_s(\theta),$$

and

$$\mathbf{S}(\mathbf{W}; \theta) = (s_1, s_2, s_3)^T = \mathbf{M}(\theta) \left( \frac{\partial \mathbf{W}}{\partial y} \cos \theta - \frac{\partial \mathbf{W}}{\partial x} \sin \theta \right), \quad (2.18)$$

where  $\mathbf{M}(\theta)$  is a  $3 \times 3$  matrix defined by

$$\mathbf{M}(\theta) = \begin{pmatrix} 0 & -M_1(\theta) & 0 \\ -M_2(\theta) & 0 & M_2(\theta) \\ 0 & M_1(\theta) & 0 \end{pmatrix}, \quad (2.19)$$

here  $M_1(\theta) = \frac{\tilde{h}}{2}$  and  $M_2(\theta) = \frac{g}{K_\theta^2 \Lambda}$ .

**Proof** Because

$$\tilde{\mathbf{B}}_i(\theta) = \tilde{\mathbf{L}}(\theta) \tilde{\mathbf{A}}_i \tilde{\mathbf{R}}(\theta), \quad i = 1, 2,$$

one has

$$\tilde{\mathbf{B}}_1(\theta) = \begin{pmatrix} \tilde{u} - \tilde{c}\tilde{G}_c(\theta) & -\frac{\tilde{h}}{2} \sin \theta & 0 \\ -\frac{1}{K_\theta^2 \Lambda} g \sin \theta & \tilde{u} & \frac{1}{K_\theta^2 \Lambda} g \sin \theta \\ 0 & \frac{\tilde{h}}{2} \sin \theta & \tilde{u} + \tilde{c}\tilde{G}_c(\theta) \end{pmatrix},$$

$$\tilde{\mathbf{B}}_2(\theta) = \begin{pmatrix} \tilde{v} - \tilde{c}\tilde{G}_s(\theta) & \frac{\tilde{h}}{2} \cos \theta & 0 \\ \frac{1}{K_\theta^2 \Lambda} g \cos \theta & \tilde{v} & -\frac{1}{K_\theta^2 \Lambda} g \cos \theta \\ 0 & -\frac{\tilde{h}}{2} \cos \theta & \tilde{v} + \tilde{c}\tilde{G}_s(\theta) \end{pmatrix}.$$

Thus the identities

$$\tilde{\mathbf{B}}_1(\theta) = \tilde{\mathbf{D}}_1(\theta) + \mathbf{M}(\theta) \sin \theta, \quad \tilde{\mathbf{B}}_2(\theta) = \tilde{\mathbf{D}}_2(\theta) - \mathbf{M}(\theta) \cos \theta, \quad (2.20)$$

holds for all  $\theta \in \mathbb{R}$ . Using (2.15) and (2.20) may complete the proof.  $\blacksquare$

**Remark 2.1** *The left-hand side of the quasi-diagonalized system (2.13) does fully decouple the components of the characteristic variable vector  $\mathbf{W} = (w_1, w_2, w_3)$ , but the right-hand side of (2.13) weakly couples three characteristic variables  $w_1, w_2$ , and  $w_3$ , that is, the  $\ell$ th component of  $\mathbf{S}(\mathbf{W}; \theta)$  in (2.13) does not depend on the characteristic variable  $w_\ell$ .*

Along the bicharacteristics (2.16), the system (2.13) reduces to the following system of ordinary differential equations

$$\frac{D^{(\ell)} w_\ell}{Dt} = s_\ell + s_\ell^{(a)}, \ell = 1, 2, 3, \quad (2.21)$$

where the differential operator  $\frac{D^{(\ell)}}{Dt} := \frac{\partial}{\partial t} + d_1^{(\ell)}(\theta) \frac{\partial}{\partial x} + d_2^{(\ell)}(\theta) \frac{\partial}{\partial y}$  denotes the total derivative operator along the  $\ell$ th bicharacteristic in (2.16). Along the  $\ell$ th bicharacteristic in (2.16), integrating the  $\ell$ th equation in (2.21) in terms of the time from  $t$  to  $t + \tau$  with  $\tau > 0$  gives the following equivalent integral system of (2.11)

$$\begin{aligned} w_\ell(x, y, t + \tau; \theta) &= w_\ell(x - d_1^{(\ell)}(\theta)\tau, y - d_2^{(\ell)}(\theta)\tau, t; \theta) \\ &\quad + s_\ell^\tau(x, y, t; \theta) + s_\ell^{\tau, (a)}(x, y, t; \theta), \end{aligned} \quad (2.22)$$

or

$$\begin{pmatrix} w_1(\mathbf{P}; \theta) \\ w_2(\mathbf{P}; \theta) \\ w_3(\mathbf{P}; \theta) \end{pmatrix} = \begin{pmatrix} w_1(\mathbf{Q}_1(\theta); \theta) + s_1^\tau(\mathbf{P}_0; \theta) + s_1^{\tau, (a)}(\mathbf{P}_0; \theta) \\ w_2(\mathbf{Q}_2(\theta); \theta) + s_2^\tau(\mathbf{P}_0; \theta) + s_2^{\tau, (a)}(\mathbf{P}_0; \theta) \\ w_3(\mathbf{Q}_3(\theta); \theta) + s_3^\tau(\mathbf{P}_0; \theta) + s_3^{\tau, (a)}(\mathbf{P}_0; \theta) \end{pmatrix}, \quad (2.23)$$

where

$$\begin{aligned} s_\ell^\tau(x, y, t; \theta) &= \int_t^{t+\tau} s_\ell(x - d_1^{(\ell)}(\theta)(t + \tau - \zeta), y - d_2^{(\ell)}(\theta)(t + \tau - \zeta), \zeta; \theta) d\zeta, \\ s_\ell^{\tau, (a)}(x, y, t; \theta) &= \int_t^{t+\tau} s_\ell^{(a)}(x - d_1^{(\ell)}(\theta)(t + \tau - \zeta), y - d_2^{(\ell)}(\theta)(t + \tau - \zeta), \zeta; \theta) d\zeta, \end{aligned} \quad (2.24)$$

and  $\mathbf{P}, \mathbf{P}_0$ , and  $\mathbf{Q}_\ell(\theta)$  denote the points  $(x, y, t + \tau)$ ,  $(x, y, t)$ , and  $(x - d_1^{(\ell)}(\theta)\tau, y - d_2^{(\ell)}(\theta)\tau, t)$ , respectively. The integral equation (2.22) or (2.23) gives the time evolution of the variable  $w_\ell$  in the quasi-diagonalized system (2.13) along its bicharacteristics (2.12),  $\ell = 1, 2, 3$ .

Multiplying (2.23) by  $\tilde{\mathbf{R}}(\theta)$  from the left and integrating it with respect to  $\theta$  from 0 to  $2\pi$  (i.e. superposition of all the waves together) yield the exact evolution operator  $\mathcal{E}(\tau)$

of (2.11) as follows

$$\mathcal{E}(\tau)\mathbf{V}(\mathbf{P}_0) := \mathbf{V}(\mathbf{P}) = \frac{1}{2\pi} \int_0^{2\pi} \sum_{\ell=1}^3 \tilde{\mathbf{R}}^{(\ell)}(\theta) \left( w_\ell(\mathbf{Q}_\ell(\theta); \theta) + s_\ell^\tau(\mathbf{P}_0; \theta) + s_\ell^{\tau, (a)}(\mathbf{P}_0; \theta) \right). \quad (2.25)$$

**Theorem 2.1** *The exact integral equations (2.25) are equivalent to*

$$h(\mathbf{P}) = \frac{1}{2\pi} \int_0^{2\pi} J d\theta - \frac{\tilde{h}}{2\pi} \int_0^{2\pi} \int_t^{t+\tau} \mathcal{S}(\mathbf{Q}_\zeta(\theta); \theta) d\zeta d\theta, \quad (2.26)$$

$$\begin{aligned} u(\mathbf{P}) &= -\frac{g}{2\pi\tilde{c}} \int_0^{2\pi} J\tilde{G}_c(\theta) d\theta + [u(\mathbf{P}')J_6 - v(\mathbf{P}')J_4] \\ &\quad + \frac{g}{\tilde{\Lambda}} \int_t^{t+\tau} \left( h_y(\mathbf{P}'_\zeta)J_1 - h_x(\mathbf{P}'_\zeta)J_2 \right) d\zeta + \frac{\tilde{c}}{2\pi} \int_0^{2\pi} \int_t^{t+\tau} \tilde{G}_c(\theta)\mathcal{S}(\mathbf{Q}_\zeta(\theta); \theta) d\zeta d\theta \\ &\quad + \frac{1}{2\pi} \int_0^{2\pi} \int_t^{t+\tau} S_1^{(1)}(\mathbf{Q}_\zeta(\theta); \theta) d\zeta d\theta, \end{aligned} \quad (2.27)$$

$$\begin{aligned} v(\mathbf{P}) &= -\frac{g}{2\pi\tilde{c}} \int_0^{2\pi} J\tilde{G}_s(\theta) d\theta - [u(\mathbf{P}')J_7 - v(\mathbf{P}')J_5] \\ &\quad + \frac{g}{\tilde{\Lambda}} \int_t^{t+\tau} \left( h_x(\mathbf{P}'_\zeta)J_1 - h_y(\mathbf{P}'_\zeta)J_3 \right) d\zeta + \frac{\tilde{c}}{2\pi} \int_0^{2\pi} \int_t^{t+\tau} \tilde{G}_s(\theta)\mathcal{S}(\mathbf{Q}_\zeta(\theta); \theta) d\zeta d\theta \\ &\quad + \frac{1}{2\pi} \int_0^{2\pi} \int_t^{t+\tau} S_1^{(2)}(\mathbf{Q}_\zeta(\theta); \theta) d\zeta d\theta, \end{aligned} \quad (2.28)$$

where  $\mathcal{S}(x, y, t; \theta) = \frac{1}{K_\theta} (\Phi_x \sin \theta - \Phi_y \cos \theta)$ ,  $\Phi_x$  and  $\Phi_y$  are the partial derivatives of  $\Phi(x, y, t; \theta) := \tilde{G}_s(\theta)u - \tilde{G}_c(\theta)v$  with respect to  $x$  and  $y$  respectively, and the shortened notations  $\mathbf{P}' := \mathbf{Q}_2$  and  $\mathbf{Q}(\theta) := \mathbf{Q}_1(\theta)$ . Moreover,  $\mathbf{Q}_\zeta(\theta)$  and  $\mathbf{P}'_\zeta$  denote the points

$$\left( x - d_1^{(1)}(\theta)(t + \tau - \zeta), y - d_2^{(1)}(\theta)(t + \tau - \zeta), \zeta \right),$$

and

$$\left( x - \tilde{u}(t + \tau - \zeta), y - \tilde{v}(t + \tau - \zeta), \zeta \right),$$

respectively. Here,  $J$  and  $J_i, i = 1, 2, \dots, 7$ , are defined by

$$J := h(\mathbf{Q}(\theta)) - \frac{\tilde{c}}{g\tilde{K}_\theta} (u(\mathbf{Q}(\theta)) \cos \theta + v(\mathbf{Q}(\theta)) \sin \theta) \quad (2.29)$$

$$J_1 := \frac{1}{2\pi} \int_0^{2\pi} \frac{\sin \theta \cos \theta}{\tilde{K}_\theta^2} d\theta = \begin{cases} 0, & \tilde{\mathbf{x}} = \mathbf{0}, \\ \frac{\tilde{g}^{12}}{H} \left( 2 - (\tilde{g}^{11} + \tilde{g}^{22}) \tilde{\Lambda} \right), & \tilde{\mathbf{x}} \neq \mathbf{0}, \end{cases} \quad (2.30)$$

$$J_2 := \frac{1}{2\pi} \int_0^{2\pi} \frac{\sin^2 \theta}{\tilde{K}_\theta^2} d\theta = \begin{cases} \frac{1}{2}, & \tilde{\mathbf{x}} = \mathbf{0}, \\ \frac{1}{H} \left( ((\tilde{g}^{11})^2 - \tilde{g}^{11}\tilde{g}^{22} + 2(\tilde{g}^{12})^2) \tilde{\Lambda} + \tilde{g}^{22} - \tilde{g}^{11} \right), & \tilde{\mathbf{x}} \neq \mathbf{0}, \end{cases} \quad (2.31)$$

$$J_3 := \frac{1}{2\pi} \int_0^{2\pi} \frac{\cos^2 \theta}{\tilde{K}_\theta^2} d\theta = \begin{cases} \frac{1}{2}, & \tilde{\mathbf{x}} = \mathbf{0}, \\ \frac{1}{H} \left( ((\tilde{g}^{22})^2 - \tilde{g}^{11}\tilde{g}^{22} + 2(\tilde{g}^{12})^2) \tilde{\Lambda} + \tilde{g}^{11} - \tilde{g}^{22} \right), & \tilde{\mathbf{x}} \neq \mathbf{0}, \end{cases} \quad (2.32)$$

$$J_4 := \frac{1}{2\pi} \int_0^{2\pi} \frac{\tilde{G}_c(\theta) \sin \theta}{\tilde{K}_\theta} d\theta = \tilde{g}^{11} J_1 + \tilde{g}^{12} J_2, \quad (2.33)$$



$$J_5 := \frac{1}{2\pi} \int_0^{2\pi} \frac{\tilde{G}_c(\theta) \cos \theta}{\tilde{K}_\theta} d\theta = \tilde{g}^{11} J_3 + \tilde{g}^{12} J_1, \quad (2.34)$$

$$J_6 := \frac{1}{2\pi} \int_0^{2\pi} \frac{\tilde{G}_s(\theta) \sin \theta}{\tilde{K}_\theta} d\theta = \tilde{g}^{12} J_1 + \tilde{g}^{22} J_2, \quad (2.35)$$

$$J_7 := \frac{1}{2\pi} \int_0^{2\pi} \frac{\tilde{G}_s(\theta) \cos \theta}{\tilde{K}_\theta} d\theta = \tilde{g}^{12} J_3 + \tilde{g}^{22} J_1, \quad (2.36)$$

with

$$\tilde{H} = (\tilde{g}^{11})^2 + (\tilde{g}^{22})^2 - 2\tilde{g}^{11}\tilde{g}^{22} + 4(\tilde{g}^{12})^2.$$

**Proof** Because the variables  $w_\ell(\mathbf{Q}_\ell(\theta); \theta)$  and  $\tilde{\mathbf{R}}^{(\ell)}(\theta)$  are  $2\pi$ -periodic with respect to  $\theta$ ,  $\ell = 1, 3$ , and

$$\tilde{\mathbf{R}}^{(1)}(\theta + \pi) = -\tilde{\mathbf{R}}^{(3)}(\theta), \quad d_i^{(1)}(\theta + \pi) = d_i^{(3)}(\theta), \quad i = 1, 2, \quad \mathbf{M}(\theta + \pi) = \mathbf{M}(\theta),$$

which imply

$$\mathbf{Q}_1(\theta + \pi) = \mathbf{Q}_3(\theta), \quad w_1(\mathbf{Q}_1(\theta + \pi); \theta + \pi) = -w_3(\mathbf{Q}_3(\theta); \theta), \quad w_2(\mathbf{P}_0; \theta + \pi) = -w_2(\mathbf{P}_0; \theta),$$

one has

$$\int_0^{2\pi} \tilde{\mathbf{R}}^{(1)}(\theta) w_1(\mathbf{Q}_1(\theta); \theta) d\theta = \int_0^{2\pi} \tilde{\mathbf{R}}^{(3)}(\theta) w_3(\mathbf{Q}_3(\theta); \theta) d\theta, \quad (2.37)$$

and

$$\begin{aligned} s_1(\mathbf{x}, t; \theta + \pi) &= M_1(\theta + \pi) \left( \frac{\partial w_2(\mathbf{x}, t; \theta + \pi)}{\partial x} \sin(\theta + \pi) - \frac{\partial w_2(\mathbf{x}, t; \theta + \pi)}{\partial y} \cos(\theta + \pi) \right) \\ &= M_1(\theta) \left( \frac{\partial w_2(\mathbf{x}, t; \theta)}{\partial x} \sin \theta - \frac{\partial w_2(\mathbf{x}, t; \theta)}{\partial y} \cos \theta \right) = -s_3(\mathbf{x}, t; \theta). \end{aligned}$$

Substituting the last equation into (2.24) gives

$$\begin{aligned} s_1^\tau(\mathbf{x}, t; \theta + \pi) &= \int_t^{t+\tau} s_1 \left( x - d_1^{(1)}(\theta + \pi)(t + \tau - \zeta), y - d_2^{(1)}(\theta + \pi)(t + \tau - \zeta), \zeta; \theta + \pi \right) d\zeta \\ &= \int_t^{t+\tau} s_1 \left( x - d_1^{(3)}(\theta)(t + \tau - \zeta), y - d_2^{(3)}(\theta)(t + \tau - \zeta), \zeta; \theta + \pi \right) d\zeta \\ &= - \int_t^{t+\tau} s_3 \left( x - d_1^{(3)}(\theta)(t + \tau - \zeta), y - d_2^{(3)}(\theta)(t + \tau - \zeta), \zeta; \theta + \pi \right) d\zeta \\ &= -s_3^\tau(\mathbf{x}, t; \theta), \end{aligned}$$

and thus the identity

$$\int_0^{2\pi} \tilde{\mathbf{R}}^{(1)}(\theta) s_1^\tau(\mathbf{x}, t; \theta) d\theta = \int_0^{2\pi} \tilde{\mathbf{R}}^{(3)}(\theta) s_3^\tau(\mathbf{x}, t; \theta) d\theta, \quad (2.38)$$

holds. With the definition of  $\tilde{\mathbf{R}}^{(\ell)}(\theta)$  and the identities (2.37) and (2.38), the exact integral

equations (2.25) can be rewritten as follows

$$\begin{aligned} \mathbf{V}(\mathbf{P}) = & \frac{1}{2\pi} \int_0^{2\pi} \left( \begin{array}{c} -2(w_1(\mathbf{Q}(\theta); \theta) + s_1^\tau(\mathbf{x}, t; \theta)) \\ 2\frac{g}{\tilde{K}_\theta} \tilde{G}_c(\theta) (w_1(\mathbf{Q}(\theta); \theta) + s_1^\tau(\mathbf{x}, t; \theta)) + (w_2(\mathbf{P}'; \theta) + s_2^\tau(\mathbf{x}, t; \theta)) \sin \theta \\ 2\frac{g}{\tilde{K}_\theta} \tilde{G}_s(\theta) (w_1(\mathbf{Q}(\theta); \theta) + s_1^\tau(\mathbf{x}, t; \theta)) - (w_2(\mathbf{P}'; \theta) + s_2^\tau(\mathbf{x}, t; \theta)) \cos \theta \end{array} \right) d\theta \\ & + \frac{1}{2\pi} \int_0^{2\pi} \int_t^{t+\tau} \mathbf{S}_1(\mathbf{Q}_\zeta(\theta); \theta) d\zeta d\theta. \end{aligned} \quad (2.39)$$

Noting the relations in (2.14) gives

$$\begin{aligned} \frac{1}{2\pi} \int_0^{2\pi} w_2(\mathbf{P}'; \theta) \sin \theta d\theta &= \frac{1}{2\pi} \int_0^{2\pi} \frac{1}{\tilde{K}_\theta} [\tilde{G}_s(\theta)u(\mathbf{P}') - \tilde{G}_c(\theta)v(\mathbf{P}')] \sin \theta d\theta \\ &= u(\mathbf{P}')J_6 - v(\mathbf{P}')J_4, \end{aligned} \quad (2.40)$$

$$\begin{aligned} \frac{1}{2\pi} \int_0^{2\pi} w_2(\mathbf{P}'; \theta) \cos \theta d\theta &= \frac{1}{2\pi} \int_0^{2\pi} \frac{1}{\tilde{K}_\theta} [\tilde{G}_s(\theta)u(\mathbf{P}') - \tilde{G}_c(\theta)v(\mathbf{P}')] \cos \theta d\theta \\ &= u(\mathbf{P}')J_7 - v(\mathbf{P}')J_5. \end{aligned} \quad (2.41)$$

On the other hand, one has

$$\begin{aligned} s_1(\mathbf{x}, t; \theta) &= -M_1(\theta) \left( \frac{\partial w_2(\mathbf{x}, t; \theta)}{\partial y} \cos \theta - \frac{\partial w_2(\mathbf{x}, t; \theta)}{\partial x} \sin \theta \right) \\ &= -\frac{1}{2}\tilde{h} \left( \frac{\partial w_2(\mathbf{x}, t; \theta)}{\partial y} \cos \theta - \frac{\partial w_2(\mathbf{x}, t; \theta)}{\partial x} \sin \theta \right) \\ &= \frac{1}{2}\tilde{h} \frac{\sin \theta}{\tilde{K}_\theta} [\tilde{G}_s(\theta)u_x - \tilde{G}_c(\theta)v_x] - \frac{1}{2}\tilde{h} \frac{\cos \theta}{\tilde{K}_\theta} [\tilde{G}_s(\theta)u_y - \tilde{G}_c(\theta)v_y], \end{aligned} \quad (2.42)$$

$$\begin{aligned} s_2(\mathbf{x}, t; \theta) &= M_2(\theta) \left( \frac{\partial(w_3 - w_1)(\mathbf{x}, t; \theta)}{\partial y} \cos \theta - \frac{\partial(w_3 - w_1)(\mathbf{x}, t; \theta)}{\partial x} \sin \theta \right) \\ &= \frac{g}{\tilde{K}_\theta^2 \tilde{\Lambda}} (-(w_3 - w_1)_x \sin \theta + (w_3 - w_1)_y \cos \theta) \\ &= \frac{g}{\tilde{K}_\theta^2 \tilde{\Lambda}} (-h_x \sin \theta + h_y \cos \theta). \end{aligned} \quad (2.43)$$

Substituting (2.40)-(2.43) into (2.39) may give the integral equations in (2.26)-(2.28). The proof is completed.  $\blacksquare$

The integral equations (2.26)-(2.28) are the base of our RKDLEG methods presented in Section 3. In order to derive the RKDLEG method, the exact evolution operator  $\mathcal{E}(\tau)$  or the integrals in (2.26)-(2.28) has to be further numerically approximated, see Section 3.3.1.

### 3 Numerical method

This section is devoted to present the RKDLEG method for the SWEs (2.6) on the cubed-sphere. Let  $x$  and  $y$  be the Cartesian coordinates in a face of the cube and restrict our attention to the following square mesh in the  $(x, y)$  plane:

$$x_j = -\frac{\pi}{4} + \frac{j\pi}{2N}, \quad y_k = -\frac{\pi}{4} + \frac{k\pi}{2N}, \quad j, k = 0, 1, \dots, N,$$

where  $N$  is the grid number in  $x$  or  $y$  direction. Moreover, the time interval  $[0, T]$  is assumed to be partitioned into  $\{t_n | t_0 = 0, t_{n+1} = t_n + \Delta t_n, n \geq 0\}$ , where  $\Delta t_n$  is the time step size determined by

$$\Delta t_n = \frac{\pi C_{cfl}}{2N \max_{j,k,1 \leq \ell \leq 3} \left\{ |\lambda^{(\ell)}(\bar{\mathbf{V}}_{j+\frac{1}{2},k+\frac{1}{2}}^n, \mathbf{x}_{j+\frac{1}{2},k+\frac{1}{2}}, 0)| + |\lambda^{(\ell)}(\bar{\mathbf{V}}_{j+\frac{1}{2},k+\frac{1}{2}}^n, \mathbf{x}_{j+\frac{1}{2},k+\frac{1}{2}}, \frac{\pi}{2})| \right\}}, \quad (3.1)$$

where  $\lambda^{(\ell)}(\mathbf{V}, \mathbf{x}; \theta)$  is given in (2.8),  $\ell = 1, 2, 3$ ,  $C_{cfl}$  denotes the CFL number, and

$$\bar{\mathbf{V}}_{j+\frac{1}{2},k+\frac{1}{2}}^n \approx \frac{4N^2}{\pi^2} \iint_{C_{j+\frac{1}{2},k+\frac{1}{2}}} \mathbf{V}(\mathbf{x}, t_n) d\mathbf{x}.$$

here the cell  $C_{j+\frac{1}{2},k+\frac{1}{2}}$  defined by

$$C_{j+\frac{1}{2},k+\frac{1}{2}} = \{(x, y) | x_j \leq x \leq x_{j+1}, y_k \leq y \leq y_{k+1}, 0 \leq j, k \leq N-1\}.$$

#### 3.1 DG spatial discretization

This section gives the DG spatial discretizations of the SWEs (2.6). The purpose is to seek an approximation  $\mathbf{U}_h$  to  $\mathbf{U}$  such that for each time  $t \in (0, T]$ , each component of  $\mathbf{U}_h$  belongs to the finite dimensional space

$$V_h := \left\{ v(\mathbf{x}) \in L^2(\tilde{\Omega}) : v(\mathbf{x})|_{C_{j+\frac{1}{2},k+\frac{1}{2}}} \in \mathbb{P}^K(C_{j+\frac{1}{2},k+\frac{1}{2}}) \right\},$$

where  $\tilde{\Omega} = [-\frac{\pi}{4}, \frac{\pi}{4}] \times [-\frac{\pi}{4}, \frac{\pi}{4}]$ ,  $\mathbb{P}^K(C_{j+\frac{1}{2},k+\frac{1}{2}})$  is the space of polynomials in the cell  $C_{j+\frac{1}{2},k+\frac{1}{2}}$  of degree at most  $K$ , with the dimension at most  $(K+1)(K+2)/2$ .

Multiplying (2.6) with a test function  $v(\mathbf{x}) \in \mathbb{P}^K(C_{j+\frac{1}{2},k+\frac{1}{2}})$ , integrating by parts over the cell  $C_{j+\frac{1}{2},k+\frac{1}{2}}$ , and replacing the exact solution  $\mathbf{U}$  with the approximate solution  $\mathbf{U}_h$  give

$$\frac{d}{dt} \iint_{C_{j+\frac{1}{2},k+\frac{1}{2}}} \mathbf{U}_h(\mathbf{x}, t) v(\mathbf{x}) d\mathbf{x} = - \int_{\partial C_{j+\frac{1}{2},k+\frac{1}{2}}} \mathbf{F}_n(\mathcal{E}_{h,0} \mathbf{V}_h(\mathbf{x}, t)) v(\mathbf{x}) ds$$

$$+ \iint_{C_{j+\frac{1}{2},k+\frac{1}{2}}} \left( \mathbf{S}_0(\mathbf{U}_h(\mathbf{x}, t))v(\mathbf{x}) + \mathbf{F}(\mathbf{U}_h(\mathbf{x}, t)) \cdot \nabla v(\mathbf{x}) \right) d\mathbf{x}, \quad (3.2)$$

where  $\mathbf{F} = (\mathbf{F}_1, \mathbf{F}_2)$ ,  $\mathbf{F}_n(\mathbf{U}) = \mathbf{F}(\mathbf{U}) \cdot \mathbf{n}$ ,  $\nabla v(\mathbf{x}) = (\partial_x, \partial_y)v(\mathbf{x})$ ,  $\mathbf{n} = (n_1, n_2)$  is the outward unit normal vector of the cell boundary  $\partial C_{j+\frac{1}{2},k+\frac{1}{2}}$ ,  $\mathcal{E}_{h,0}$  is the approximate local evolution operator and will be discussed in Section 3.3, and  $\mathbf{V}_h(\mathbf{x}, t)$  is the primitive variable vector corresponding to  $\mathbf{U}_h(\mathbf{x}, t)$ . It is worth noting that in the traditional RKDG method for hyperbolic conservation laws, see e.g. [8], the first term at the right-hand side of (3.2) is replaced with

$$- \int_{\partial C_{j+\frac{1}{2},k+\frac{1}{2}}} \widehat{\mathbf{F}}_n(\mathbf{U}_h(\mathbf{x} - 0, t), \mathbf{U}_h(\mathbf{x} + 0, t)) v(\mathbf{x}) ds,$$

where  $\widehat{\mathbf{F}}_n(\cdot, \cdot)$  is the two-point numerical flux vector satisfying the consistency condition  $\widehat{\mathbf{F}}_n(\mathbf{U}, \mathbf{U}) = \mathbf{F}_n(\mathbf{U})$ .

If using  $\{\phi_{j,k}^{(\ell)}(\mathbf{x}), \ell = 0, 1, \dots, K(K+3)/2\}$  to denote a basis of the space  $\mathbb{P}^K(C_{j+\frac{1}{2},k+\frac{1}{2}})$ , then the DG approximate solution  $\mathbf{U}_h$  may be expressed by

$$\mathbf{U}_h(\mathbf{x}, t) = \sum_{\ell=0}^{K(K+3)/2} \mathbf{U}_{j,k}^{(\ell)}(t) \phi_{j,k}^{(\ell)}(\mathbf{x}), \text{ if } \mathbf{x} \in C_{j+\frac{1}{2},k+\frac{1}{2}}, \quad (3.3)$$

and the scaled Legendre polynomials are taken as the basis in this paper, see Section 3.3.2 in [53].

The first and second terms at the right-hand side of (3.2) are further respectively discretized by using Gaussian quadratures of high order accuracy as follows

$$- |\partial C_{j+\frac{1}{2},k+\frac{1}{2}}| \sum_{m=1}^{K+2} \tilde{\omega}_m \mathbf{F}_n(\mathcal{E}_{h,0} \mathbf{V}_h(\tilde{\mathbf{x}}_m^G, t)) v(\tilde{\mathbf{x}}_m^G) ds, \quad (3.4)$$

$$|C_{j+\frac{1}{2},k+\frac{1}{2}}| \sum_{m=1}^{(K+2)^2} \omega_m \left( \mathbf{F}(\mathbf{U}_h(\mathbf{x}_m^G, t)) \cdot \nabla v(\mathbf{x}_m^G) + \mathbf{S}_0(\mathbf{U}_h(\mathbf{x}_m^G, t)) v(\mathbf{x}_m^G) \right), \quad (3.5)$$

where  $\{\tilde{\omega}_m, \tilde{\mathbf{x}}_m^G\}$ ,  $m = 1, \dots, K+2$ , and  $\{\omega_m, \mathbf{x}_m^G\}$ ,  $m = 1, \dots, (K+2)^2$ , denote the Gauss-Lobatto quadrature weights and nodes in  $\partial C_{j+\frac{1}{2},k+\frac{1}{2}}$  and  $C_{j+\frac{1}{2},k+\frac{1}{2}}$ , respectively.

In conclusion, our semi-discrete  $\mathbb{P}^K$ -based DG methods for (2.6) may be given as

$$\begin{aligned} \sum_{\ell=0}^{K(K+3)/2} \iint_{C_{j+\frac{1}{2},k+\frac{1}{2}}} \phi_{j,k}^{(\ell)} v(\mathbf{x}) d\mathbf{x} \frac{d\mathbf{U}_{j,k}^{(\ell)}(t)}{dt} &= - |\partial C_{j+\frac{1}{2},k+\frac{1}{2}}| \sum_{m=1}^{K+2} \tilde{\omega}_m \mathbf{F}_n(\mathcal{E}_{h,0} \mathbf{V}_h(\tilde{\mathbf{x}}_m^G, t)) v(\tilde{\mathbf{x}}_m^G) \\ &+ |C_{j+\frac{1}{2},k+\frac{1}{2}}| \sum_{m=1}^{(K+2)^2} \omega_m \left( \mathbf{F}(\mathbf{U}_h(\mathbf{x}_m^G, t)) \cdot \nabla v(\mathbf{x}_m^G) + \mathbf{S}_0(\mathbf{U}_h(\mathbf{x}_m^G, t)) v(\mathbf{x}_m^G) \right), \end{aligned} \quad (3.6)$$

for  $v(\mathbf{x}) = \phi_{j,k}^{(\ell')}(\mathbf{x})$ ,  $\ell' = 0, 1, \dots, K(K+3)/2$ . It forms a nonlinear system of ordinary differential equations evolving the degrees of freedom or moments  $\mathbf{U}_{j,k}^{(\ell)}(t)$ ,  $\ell =$

$0, 1, \dots, K(K+3)/2$ .

### 3.2 Time discretization

The semi-discrete schemes (3.6) may be rewritten into an abstract form

$$\frac{d\mathbf{U}}{dt} = \mathbf{L}(\mathbf{U}, t), \quad (3.7)$$

which is a nonlinear system of ordinary differential equations with respect to  $\mathbf{U}$ . Following the traditional RKDG methods, the system (3.7) may be approximated by some strong stability-preserving high-order time discretization. For example, the explicit third order Runge-Kutta discretization [40] for (3.7) may be given by

$$\begin{aligned} \mathbf{U}^{(1)} &= \mathbf{U}^n + \Delta t_n \mathbf{L}(\mathbf{U}^n, t_n), \\ \mathbf{U}^{(2)} &= \frac{3}{4} \mathbf{U}^n + \frac{1}{4} \left( \mathbf{U}^{(1)} + \Delta t_n \mathbf{L}(\mathbf{U}^{(1)}, t_n + \Delta t_n) \right), \\ \mathbf{U}^{n+1} &= \frac{1}{3} \mathbf{U}^n + \frac{2}{3} \left( \mathbf{U}^{(2)} + \Delta t_n \mathbf{L}(\mathbf{U}^{(2)}, t_n + \frac{1}{2} \Delta t_n) \right). \end{aligned}$$

In our practical computations, in order to match the accuracy of DG spatial discretization, the  $(K+1)$ th order strong stability-preserving explicit Runge-Kutta method is used for the  $\mathbb{P}^K$ -based RKDLEG methods,  $K=1, 2$ , but a general explicit fourth-order explicit Runge-Kutta method is employed for the  $\mathbb{P}^3$ -based RKDLEG methods.

### 3.3 Approximate evolution operators

This section will derive the approximate local evolution operator  $\mathcal{E}_{h,0}$  used in our RKDLEG methods, see (3.6). The operator  $\mathcal{E}_{h,0}$  is the limit of the approximate evolution operator  $\mathcal{E}_h(\tau)$  as  $\tau$  approaches to zero, i.e.  $\mathcal{E}_{h,0} = \lim_{\tau \rightarrow 0} \mathcal{E}_h(\tau)$ , where  $\mathcal{E}_h(\tau)$  is an appropriate approximation of the exact evolution operator  $\mathcal{E}(\tau)$  defined in (2.25) by numerically approximating the ‘‘source’’ terms in (2.26)-(2.28), specifically, the integrands of the integral terms depending on  $\mathcal{S}(\mathbf{Q}_\zeta(\theta); \theta)$ ,  $S_1^{(1)}(\mathbf{Q}_\zeta(\theta); \theta)$ , and  $S_1^{(2)}(\mathbf{Q}_\zeta(\theta); \theta)$ .

#### 3.3.1 Approximate evolution operator $\mathcal{E}_h(\tau)$

Our RKDLEG methods only require the approximate local evolution operator  $\mathcal{E}_{h,0}$  at the Gauss-Lobatto quadrature nodes. Without loss of generality, we will only discuss the (approximate) evolution operator at the grid point  $(x_j, y_k)$  (not on the edges of the cube face). The inner points on the cell edge  $\partial C_{j+\frac{1}{2}, k+\frac{1}{2}}$  will be similarly discussed and simpler than those grid points. Assume that the coordinates points  $P_0$  and  $P$  in Fig. 2.2 are  $(x_j, y_k, t_n)$

and  $(x_j, y_k, t_n + \tau)$  with  $0 < \tau \leq \Delta t_n$ . Such constraint on  $\tau$  guarantees that the bicharacteristic cones past the Gauss-Lobatto quadrature nodes do not interact with each other. Use  $\mathcal{C}_P^n$  to denote the close curve  $\{(x_j - d_1^{(\ell)}(\theta)\tau, y_k - d_2^{(\ell)}(\theta)\tau, t_n) =: \mathbf{Q}(\theta) | \ell = 1, 3, \theta \in [0, 2\pi)\}$ , which are the intersection of bicharacteristic cone past the point P defined by

$$\{(x_j - d_1^{(\ell)}(\theta)\zeta, y_k - d_2^{(\ell)}(\theta)\zeta, t_n + \tau - \zeta), \ell = 1, 3, \theta \in [0, 2\pi), \zeta \in [0, \tau]\},$$

with the  $(\mathbf{x}, t_n)$  plane. Under the assumption of  $0 < \tau \leq \Delta t_n$ , the closed curve  $\mathcal{C}_P^n$  possibly intersects with following four cell edges past the grid point  $P_0$

$$\begin{aligned} \mathcal{L}_{P_0}^{(1)} &= \{(x, y_k) | x_{j-1} \leq x \leq x_j\}, \quad \mathcal{L}_{P_0}^{(2)} = \{(x_j, y) | y_{k-1} \leq y \leq y_k\}, \\ \mathcal{L}_{P_0}^{(3)} &= \{(x, y_k) | x_j \leq x \leq x_{j+1}\}, \quad \mathcal{L}_{P_0}^{(4)} = \{(x_j, y) | y_k \leq y \leq y_{k+1}\}. \end{aligned}$$

In the following, the notation  $\hat{N}$  will be used to denote the number of the arc segments of the closed curve  $\mathcal{C}_P^n$ . Use  $\theta_i$  to denote the angle corresponding to the  $i$ th intersection point between  $\mathcal{C}_P^n$  and  $\{\mathcal{L}_{P_0}^{(\ell)}, \ell = 1, 2, 3, 4\}$  so that the  $i$ th intersection point is  $\mathbf{Q}(\theta_i)$ ,  $i = 1, 2, \dots, \hat{N}$ , and the closed curve  $\mathcal{C}_P^n$  is divided into  $\hat{N}$  arc segments, i.e. “arc  $\mathbf{Q}(\theta_i)\mathbf{Q}(\theta_{i+1})$ ”,  $i = 1, 2, \dots, \hat{N}$ , with  $\theta_{\hat{N}+1} = \theta_1 + 2\pi$ . Calculation of  $\theta_i$  is presented in Appendix A, where the case of inner points on the edge  $\partial C_{j+\frac{1}{2}, k+\frac{1}{2}}$  is also included.

From the exact integral equations (2.26)-(2.28), one may derive the approximate integral equations or the approximate evolution operator  $\mathcal{E}_h(\tau)$  for the linearized system (2.11) as follows.

**Theorem 3.1** *The linearized system (2.11) has the approximate evolution operator  $\mathcal{E}_h(\tau)$  defined by*

$$\mathcal{E}_h(\tau)\mathbf{V}(P_0) = (h_{EG}(P), u_{EG}(P), v_{EG}(P))^T,$$

with

$$h_{EG}(P) = \frac{1}{2\pi} \sum_{i=1}^{\hat{N}} \int_{\theta_i}^{\theta_{i+1}} J d\theta - \frac{\tilde{c}\tilde{\Lambda}}{2\pi g} \sum_{i=1}^{\hat{N}} \Pi_0^i(\tau), \quad (3.8)$$

$$\begin{aligned} u_{EG}(P) &= -\frac{g}{2\pi\tilde{c}} \sum_{i=1}^{\hat{N}} \int_{\theta_i}^{\theta_{i+1}} J\tilde{G}_c(\theta) d\theta + [u(P')J_6 - v(P')J_4] \\ &\quad + \frac{\tilde{\Lambda}}{2\pi} \sum_{i=1}^{\hat{N}} \Pi_c^i(\tau) + \frac{1}{2\pi} \sum_{i=1}^{\hat{N}} \Pi_1^i(\tau) + \frac{1}{\Lambda} [(\tilde{g}_{12}J_1 - \tilde{g}_{11}J_2)(u(P') - u(P) + \tau S_1^{(1)}(P')) \\ &\quad + (\tilde{g}_{22}J_1 - \tilde{g}_{12}J_2)(v(P') - v(P) + \tau S_1^{(2)}(P'))], \quad (3.9) \end{aligned}$$

$$\begin{aligned} v_{EG}(P) &= -\frac{g}{2\pi\tilde{c}} \sum_{i=1}^{\hat{N}} \int_{\theta_i}^{\theta_{i+1}} J\tilde{G}_s(\theta) d\theta - [u(P')J_7 - v(P')J_5] \\ &\quad + \frac{\tilde{\Lambda}}{2\pi} \sum_{i=1}^{\hat{N}} \Pi_s^i(\tau) + \frac{1}{2\pi} \sum_{i=1}^{\hat{N}} \Pi_2^i(\tau) + \frac{1}{\Lambda} [(\tilde{g}_{11}J_1 - \tilde{g}_{12}J_3)(u(P') - u(P) + \tau S_1^{(1)}(P')) \\ &\quad + (\tilde{g}_{12}J_1 - \tilde{g}_{22}J_3)(v(P') - v(P) + \tau S_1^{(2)}(P'))], \quad (3.10) \end{aligned}$$

where

$$\begin{aligned}
\Pi_0^i(\tau) &= \int_{\theta_i}^{\theta_{i+1}} (\phi_1'(\theta)u(\mathbf{Q}(\theta)) - \phi_2'(\theta)v(\mathbf{Q}(\theta))) d\theta, \\
\Pi_c^i(\tau) &= \int_{\theta_i}^{\theta_{i+1}} (\phi_3'(\theta)u(\mathbf{Q}(\theta)) - \phi_4'(\theta)v(\mathbf{Q}(\theta))) d\theta, \\
\Pi_s^i(\tau) &= \int_{\theta_i}^{\theta_{i+1}} (\phi_5'(\theta)u(\mathbf{Q}(\theta)) - \phi_6'(\theta)v(\mathbf{Q}(\theta))) d\theta, \\
\Pi_1^i(\tau) &= \tau \int_{\theta_i}^{\theta_{i+1}} S_1^{(1)}(\mathbf{Q}(\theta); \theta) d\theta, \quad \Pi_2^i(\tau) = \tau \int_{\theta_i}^{\theta_{i+1}} S_1^{(2)}(\mathbf{Q}(\theta); \theta) d\theta.
\end{aligned} \tag{3.11}$$

Here

$$\begin{aligned}
\phi_1 &:= \tilde{K}_\theta^2 \tilde{G}_s(\theta), \quad \phi_2 := \tilde{K}_\theta^2 \tilde{G}_c(\theta), \quad \phi_3 := \tilde{G}_c(\theta) \phi_1(\theta), \\
\phi_4 &:= \tilde{G}_c(\theta) \phi_2(\theta), \quad \phi_5 := \tilde{G}_s(\theta) \phi_1(\theta), \quad \phi_6 := \tilde{G}_s(\theta) \phi_2(\theta).
\end{aligned}$$

Before proving Theorem 3.1, the following lemma is first introduced.

**Lemma 3.1** *If  $\phi(\theta) \in C^1(\mathbb{R})$  and  $\psi(\mathbf{x}, t)$  is continuous and differentiable along the arc segment “arc  $\mathbf{Q}(\theta_i)\mathbf{Q}(\theta_{i+1})$ ”,  $i = 1, 2, \dots, \hat{N}$ ,  $\theta_{\hat{N}+1} = \theta_1 + 2\pi$ , then the integral relation*

$$\frac{\tilde{c}\tau}{\tilde{\Lambda}} \int_0^{2\pi} \frac{\phi(\theta)}{\tilde{K}_\theta^3} (\sin \theta \psi_x(\mathbf{Q}(\theta)) - \cos \theta \psi_y(\mathbf{Q}(\theta))) d\theta = \int_0^{2\pi} \phi'(\theta) \psi(\mathbf{Q}(\theta)) d\theta, \tag{3.12}$$

holds, where  $\psi_x$  and  $\psi_y$  denote generalized derivatives of  $\psi$ .

**Proof** Integrating  $\frac{d}{d\theta} (\phi(\theta) \psi(\mathbf{Q}(\theta)))$  along the the closed curve  $\mathcal{C}_p^n$  and using the relations

$$\frac{d}{d\theta} d_1^{(1)}(\theta) = \frac{\tilde{c}}{\tilde{\Lambda} \tilde{K}_\theta^3} \sin \theta, \quad \frac{d}{d\theta} d_2^{(1)}(\theta) = -\frac{\tilde{c}}{\tilde{\Lambda} \tilde{K}_\theta^3} \cos \theta,$$

gives

$$\begin{aligned}
&\frac{\tilde{c}\tau}{\tilde{\Lambda}} \int_0^{2\pi} \frac{\phi(\theta)}{\tilde{K}_\theta^3} (\sin \theta \psi_x(\mathbf{Q}(\theta)) - \cos \theta \psi_y(\mathbf{Q}(\theta))) d\theta - \int_0^{2\pi} \phi'(\theta) \psi(\mathbf{Q}(\theta)) d\theta \\
&= - \int_0^{2\pi} (\phi(\theta) \psi(\mathbf{Q}(\theta)))' d\theta = -\phi(\theta) \psi(\mathbf{Q}(\theta)) \Big|_0^{2\pi} = 0.
\end{aligned}$$

The proof is completed. ■

**Proof of Theorem 3.1** It is divided into two steps.

**Step 1.** Let us consider both integrals depending on the height gradient  $(\partial_x h, \partial_y h)$  in (2.27) and (2.28). The linearized system (2.11) may give

$$\begin{pmatrix} \partial_x h \\ \partial_y h \end{pmatrix} = \tilde{\mathbf{L}} \left( \frac{\tilde{\mathbf{D}}\mathbf{u}}{\tilde{\mathbf{D}}t} - \begin{pmatrix} S_1^{(1)} \\ S_1^{(2)} \end{pmatrix} \right), \tag{3.13}$$



where

$$\mathbf{u} = (u, v)^T, \quad \frac{\tilde{\mathbf{D}}}{\tilde{\mathbf{D}}t} = \partial_t + \tilde{u}\partial_x + \tilde{v}\partial_y, \quad \tilde{\mathbf{L}} = -\frac{1}{g} \begin{pmatrix} \tilde{g}_{11} & \tilde{g}_{12} \\ \tilde{g}_{12} & \tilde{g}_{22} \end{pmatrix}.$$

Hence

$$\begin{aligned} & \int_{t_n}^{t_n+\tau} \begin{pmatrix} \partial_x h(\mathbf{P}'_\zeta) \\ \partial_y h(\mathbf{P}'_\zeta) \end{pmatrix} d\zeta = \tilde{\mathbf{L}} \left( \frac{\tilde{\mathbf{D}}\mathbf{u}}{\tilde{\mathbf{D}}t} \Big|_{\mathbf{P}'_\zeta} d\zeta - \int_{t_n}^{t_n+\tau} \begin{pmatrix} S_1^{(1)}(\mathbf{P}'_\zeta) \\ S_1^{(2)}(\mathbf{P}'_\zeta) \end{pmatrix} d\zeta \right) \\ &= \tilde{\mathbf{L}} \left( \frac{d}{d\zeta} \mathbf{u}(\mathbf{P}'_\zeta) d\zeta - \int_{t_n}^{t_n+\tau} \begin{pmatrix} S_1^{(1)}(\mathbf{P}'_\zeta) \\ S_1^{(2)}(\mathbf{P}'_\zeta) \end{pmatrix} d\zeta \right) = \tilde{\mathbf{L}} \left( (\mathbf{u}(\mathbf{P}) - \mathbf{u}(\mathbf{P}')) - \int_{t_n}^{t_n+\tau} \begin{pmatrix} S_1^{(1)}(\mathbf{P}'_\zeta) \\ S_1^{(2)}(\mathbf{P}'_\zeta) \end{pmatrix} d\zeta \right) \\ &= \left( \frac{1}{g} \left[ \tilde{g}_{11} (u(\mathbf{P}') - u(\mathbf{P}) + \int_{t_n}^{t_n+\tau} S_1^{(1)}(\mathbf{P}'_\zeta) d\zeta) + \tilde{g}_{12} (v(\mathbf{P}') - v(\mathbf{P}) + \int_{t_n}^{t_n+\tau} S_1^{(2)}(\mathbf{P}'_\zeta) d\zeta) \right] \right. \\ & \quad \left. + \frac{1}{g} \left[ \tilde{g}_{12} (u(\mathbf{P}') - u(\mathbf{P}) + \int_{t_n}^{t_n+\tau} S_1^{(1)}(\mathbf{P}'_\zeta) d\zeta) + \tilde{g}_{22} (v(\mathbf{P}') - v(\mathbf{P}) + \int_{t_n}^{t_n+\tau} S_1^{(2)}(\mathbf{P}'_\zeta) d\zeta) \right] \right), \end{aligned} \quad (3.14)$$

here we have used the fact that

$$\frac{d}{d\zeta} \mathbf{u}(\mathbf{P}'_\zeta) = \frac{d}{d\zeta} \mathbf{u}((x - \tilde{u}(t_n + \tau - \zeta), y - \tilde{v}(t_n + \tau - \zeta)), \zeta) = \frac{\tilde{\mathbf{D}}\mathbf{u}}{\tilde{\mathbf{D}}t} \Big|_{\mathbf{P}'_\zeta}.$$

**Step 2.** First, approximate three double integrals containing  $S(\mathbf{Q}_\zeta(\theta); \theta)$  in (2.26)-(2.28), two double integrals dependent on  $S_1^{(1)}(\mathbf{Q}_\zeta(\theta); \theta)$  and  $S_1^{(2)}(\mathbf{Q}_\zeta(\theta); \theta)$ , two single integrals relying on  $S_1^{(1)}(\mathbf{P}'_\zeta)$  and  $S_1^{(2)}(\mathbf{P}'_\zeta)$  in (3.14) with the left rectangle rule in the  $\zeta$ -direction as follows

$$\int_0^{2\pi} \int_{t_n}^{t_n+\tau} \mathcal{S}(\mathbf{Q}_\zeta(\theta); \theta) d\zeta d\theta \approx \tau \int_0^{2\pi} \mathcal{S}(\mathbf{Q}(\theta); \theta) d\theta, \quad (3.15)$$

$$\int_0^{2\pi} \int_{t_n}^{t_n+\tau} \tilde{G}_c(\theta) \mathcal{S}(\mathbf{Q}_\zeta(\theta); \theta) d\zeta d\theta \approx \tau \int_0^{2\pi} \tilde{G}_c(\theta) \mathcal{S}(\mathbf{Q}(\theta); \theta) d\theta, \quad (3.16)$$

$$\int_0^{2\pi} \int_{t_n}^{t_n+\tau} \tilde{G}_s(\theta) \mathcal{S}(\mathbf{Q}_\zeta(\theta); \theta) d\zeta d\theta \approx \tau \int_0^{2\pi} \tilde{G}_s(\theta) \mathcal{S}(\mathbf{Q}(\theta); \theta) d\theta, \quad (3.17)$$

$$\int_0^{2\pi} \int_{t_n}^{t_n+\tau} S_1^{(\ell)}(\mathbf{Q}_\zeta(\theta); \theta) d\zeta d\theta \approx \tau \int_0^{2\pi} S_1^{(\ell)}(\mathbf{Q}(\theta); \theta) d\theta, \quad \ell = 1, 2, \quad (3.18)$$

$$\int_{t_n}^{t_n+\tau} S_1^{(\ell)}(\mathbf{P}'_\zeta) d\zeta \approx \tau S_1^{(\ell)}(\mathbf{P}'), \quad \ell = 1, 2. \quad (3.19)$$

Next, use Lemma 3.1 to handle three integrals depending on the spatial derivatives of  $\mathbf{V}$

at the right-hand sides of (2.26)-(2.28). Taking  $\psi = u$  and  $\phi(\theta) = \phi_1(\theta)$  in (3.12) gives

$$\frac{\tilde{c}\tau}{\tilde{\Lambda}} \int_0^{2\pi} \frac{\tilde{G}_s(\theta)}{\tilde{K}_\theta} (\sin \theta u_x(\mathbf{Q}(\theta)) - \cos \theta u_y(\mathbf{Q}(\theta))) d\theta = \int_0^{2\pi} \phi_1'(\theta) u(\mathbf{Q}(\theta)) d\theta.$$

Again taking  $\psi = v$ ,  $\phi(\theta) = \phi_2(\theta)$  in (3.12) leads to

$$\frac{\tilde{c}\tau}{\tilde{\Lambda}} \int_0^{2\pi} \frac{\tilde{G}_c(\theta)}{\tilde{K}_\theta} (\sin \theta v_x(\mathbf{Q}(\theta)) - \cos \theta v_y(\mathbf{Q}(\theta))) d\theta = \int_0^{2\pi} \phi_2'(\theta) v(\mathbf{Q}(\theta)) d\theta.$$

Subtracting those two equations gives

$$\tau \int_0^{2\pi} \mathcal{S}(\mathbf{Q}(\theta); \theta) d\theta = \frac{\tilde{\Lambda}}{\tilde{c}} \int_0^{2\pi} (\phi_1'(\theta) u(\mathbf{Q}(\theta)) - \phi_2'(\theta) v(\mathbf{Q}(\theta))) d\theta = \frac{\tilde{\Lambda}}{\tilde{c}} \sum_{i=1}^{\hat{N}} \Pi_0^i(\tau).$$

Similarly using Lemma 3.1 may get

$$\begin{aligned} \tau \int_0^{2\pi} \tilde{G}_c(\theta) \mathcal{S}(\mathbf{Q}(\theta); \theta) d\theta &= \frac{\tilde{\Lambda}}{\tilde{c}} \int_0^{2\pi} (\phi_3'(\theta) u(\mathbf{Q}(\theta)) - \phi_4'(\theta) v(\mathbf{Q}(\theta))) d\theta = \frac{\tilde{\Lambda}}{\tilde{c}} \sum_{i=1}^{\hat{N}} \Pi_c^i(\tau), \\ \tau \int_0^{2\pi} \tilde{G}_s(\theta) \mathcal{S}(\mathbf{Q}(\theta); \theta) d\theta &= \frac{\tilde{\Lambda}}{\tilde{c}} \int_0^{2\pi} (\phi_5'(\theta) u(\mathbf{Q}(\theta)) - \phi_6'(\theta) v(\mathbf{Q}(\theta))) d\theta = \frac{\tilde{\Lambda}}{\tilde{c}} \sum_{i=1}^{\hat{N}} \Pi_s^i(\tau). \end{aligned}$$

Because the closed curve  $\mathcal{C}_p^n$  is divided into  $\hat{N}$  arc segments and the approximate solution  $\mathbf{V}_h(\mathbf{x}, t_n)$  smooth along each arc segment of  $\mathcal{C}_p^n$ , combining the above three relations with (3.14)-(3.19) as well as (2.26)-(2.28) may completes the proof of Theorem 3.1.  $\blacksquare$

**Remark 3.1** *The approximate integral equations (3.9)-(3.10) form a  $2 \times 2$  system of the linear algebraic equations with respect to the unknowns  $(u_h(\mathbf{P}), v_h(\mathbf{P}))$ . Solving this linear system may give the explicit expression of the approximate evolution operator  $\mathcal{E}_h(\tau)$ . However, it still contains the complicate integrals with respect to  $\theta$  so that the calculation of flux integral at the right-hand side of (3.6) is very time-consuming and technical. In order to avoid such difficulty, the approximate local evolution operator  $\mathcal{E}_{h,0}$  is introduced to replace  $\mathcal{E}_h(\tau)$ , see [42, 50].*

### 3.3.2 Approximate local evolution operator $\mathcal{E}_{h,0}$

This section derives the approximate local evolution operator  $\mathcal{E}_{h,0}$  defined by

$$\mathcal{E}_{h,0} := \lim_{\tau \rightarrow 0^+} \mathcal{E}_h(\tau),$$

which only requires to evolve the solutions to the time  $t_n + \tau$  from the ‘‘initial’’ time  $t_n$ , where  $0 < \tau \ll 1$ . Since the coordinates of  $\mathbf{P}'$  and  $\mathbf{Q}(\theta)$  are  $(x_j - \tilde{u}\tau, y_k - \tilde{v}\tau, t_n)$  and  $(x_j - d_1^{(1)}(\theta)\tau, y_k - d_2^{(1)}(\theta)\tau, t_n)$ , respectively, both  $\mathbf{P}'$  and  $\mathbf{Q}(\theta)$  will tend to the point  $\mathbf{P}_0$ , and the length of the arc segment ‘‘arc  $\mathbf{Q}(\theta_i) \mathbf{Q}(\theta_{i+1})$ ’’ will also approach to zero, as  $\tau \rightarrow 0^+$ .

Hence, one has

$$\begin{aligned}\lim_{\tau \rightarrow 0^+} \Pi_0^i(\tau) &= \lim_{\tau \rightarrow 0^+} \int_{\theta_i}^{\theta_{i+1}} (\phi_1'(\theta)u(\mathbf{Q}(\theta)) - \phi_2'(\theta)v(\mathbf{Q}(\theta))) d\theta \\ &= u_i^* (\phi_1(\theta_{i+1}) - \phi_1(\theta_i)) - v_i^* (\phi_2(\theta_{i+1}) - \phi_2(\theta_i)) =: \Pi_{0,0}^i,\end{aligned}$$

where

$$\mathbf{V}_i^* = (h_i^*, u_i^*, v_i^*)^T := \lim_{\tau \rightarrow 0^+} \mathbf{V}(\mathbf{Q}(\theta)), \theta \in (\theta_i, \theta_{i+1}), i = 1, 2, \dots, \hat{N}.$$

Similarly, one may also get

$$\begin{aligned}\lim_{\tau \rightarrow 0^+} \Pi_c^i(\tau) &= u_i^* (\phi_3(\theta_{i+1}) - \phi_3(\theta_i)) - v_i^* (\phi_4(\theta_{i+1}) - \phi_4(\theta_i)) =: \Pi_{c,0}^i, \\ \lim_{\tau \rightarrow 0^+} \Pi_s^i(\tau) &= u_i^* (\phi_5(\theta_{i+1}) - \phi_5(\theta_i)) - v_i^* (\phi_6(\theta_{i+1}) - \phi_6(\theta_i)) =: \Pi_{s,0}^i,\end{aligned}$$

and

$$\lim_{\tau \rightarrow 0} \Pi_1^i(\tau) = \lim_{\tau \rightarrow 0} \tau \int_{\theta_i}^{\theta_{i+1}} S_1^{(\ell)}(\mathbf{Q}(\theta); \theta) d\theta = 0, \ell = 1, 2.$$

In view of the above facts, taking the limit of the approximate integral equations (3.8)-(3.10) as  $\tau \rightarrow 0^+$  leads to the following approximate local integral equations

$$h_{LEG}(\mathbf{P}) = \frac{1}{2\pi} \sum_{i=1}^{\hat{N}} \left[ h_i^* - \frac{\tilde{c}}{g} \left( u_i^* \int_{\theta_i}^{\theta_{i+1}} \frac{\cos \theta}{\tilde{K}_\theta} d\theta + v_i^* \int_{\theta_i}^{\theta_{i+1}} \frac{\sin \theta}{\tilde{K}_\theta} d\theta \right) \right] - \frac{\tilde{c}\tilde{\Lambda}}{2\pi g} \sum_{i=1}^{\hat{N}} \Pi_{0,0}^i, \quad (3.20)$$

$$\begin{aligned}u_{LEG}(\mathbf{P}) &= \frac{g}{2\pi\tilde{c}} \sum_{i=1}^{\hat{N}} \left[ -h_i^* \int_{\theta_i}^{\theta_{i+1}} \tilde{G}_c(\theta) d\theta + \frac{\tilde{c}}{g} \left( u_i^* \int_{\theta_i}^{\theta_{i+1}} \frac{\tilde{G}_c(\theta) \cos \theta}{\tilde{K}_\theta} d\theta + v_i^* \int_{\theta_i}^{\theta_{i+1}} \frac{\tilde{G}_c(\theta) \sin \theta}{\tilde{K}_\theta} d\theta \right) \right] \\ &\quad + \frac{1}{\tilde{\Lambda}} [(\tilde{g}_{12}J_1 - \tilde{g}_{11}J_2)(u_0^* - u_h(\mathbf{P})) + (\tilde{g}_{22}J_1 - \tilde{g}_{12}J_2)(v_0^* - v_h(\mathbf{P}))] \\ &\quad + [u_0^*J_6 - v_0^*J_4] + \frac{\tilde{\Lambda}}{2\pi} \sum_{i=1}^{\hat{N}} \Pi_{c,0}^i,\end{aligned} \quad (3.21)$$

$$\begin{aligned}v_{LEG}(\mathbf{P}) &= \frac{g}{2\pi\tilde{c}} \sum_{i=1}^{\hat{N}} \left[ -h_i^* \int_{\theta_i}^{\theta_{i+1}} \tilde{G}_s(\theta) d\theta + \frac{\tilde{c}}{g} \left( u_i^* \int_{\theta_i}^{\theta_{i+1}} \frac{\tilde{G}_s(\theta) \cos \theta}{\tilde{K}_\theta} d\theta + v_i^* \int_{\theta_i}^{\theta_{i+1}} \frac{\tilde{G}_s(\theta) \sin \theta}{\tilde{K}_\theta} d\theta \right) \right] \\ &\quad + \frac{1}{\tilde{\Lambda}} [(\tilde{g}_{11}J_1 - \tilde{g}_{12}J_3)(u_0^* - u_h(\mathbf{P})) + (\tilde{g}_{12}J_1 - \tilde{g}_{22}J_3)(v_0^* - v_h(\mathbf{P}))] \\ &\quad + [u_0^*J_7 - v_0^*J_5] + \frac{\tilde{\Lambda}}{2\pi} \sum_{i=1}^{\hat{N}} \Pi_{s,0}^i,\end{aligned} \quad (3.22)$$

where

$$(h_0^*, u_0^*, v_0^*)^T = \mathbf{V}_0^* := \lim_{\tau \rightarrow 0^+} \mathbf{V}_h(\mathbf{P}'),$$

and  $\mathbf{V}_h$  is the approximate solutions in primitive variable of the RKDLEG methods. Eqs. (3.20)-(3.22) define our approximate local evolution operator, i.e.

$$\mathcal{E}_{h,0} \mathbf{V}(\mathbf{P}_0) := \mathbf{V}_{LEG}(\mathbf{P}) = (h_{LEG}(\mathbf{P}), u_{LEG}(\mathbf{P}), v_{LEG}(\mathbf{P}))^T,$$

implicitly.

**Remark 3.2** All integrals with regard to  $\theta$  at the right-hand sides of (3.20)-(3.22) can be exactly evaluated. In fact, the integrands in those integrals are

$$\frac{\cos \theta}{\tilde{K}_\theta}, \frac{\sin \theta}{\tilde{K}_\theta}, \frac{\tilde{G}_c(\theta) \cos \theta}{\tilde{K}_\theta}, \frac{\tilde{G}_c(\theta) \sin \theta}{\tilde{K}_\theta}, \frac{\tilde{G}_s(\theta) \cos \theta}{\tilde{K}_\theta}, \frac{\tilde{G}_s(\theta) \sin \theta}{\tilde{K}_\theta}, \tilde{G}_c(\theta), \tilde{G}_s(\theta),$$

whose antiderivatives or primitive functions may be gotten with the aid of the following identities

$$\begin{aligned} \int^\theta \frac{\sin \tilde{\theta} \cos \tilde{\theta}}{\lambda_1 \cos^2 \tilde{\theta} + \lambda_2 \sin^2 \tilde{\theta}} d\tilde{\theta} &= \begin{cases} -\frac{\cos^2 \theta}{2\lambda_1}, & \lambda_1 = \lambda_2, \\ \frac{\ln(\lambda_1 \cos^2 \theta + \lambda_2 \sin^2 \theta)}{2(\lambda_2 - \lambda_1)}, & \lambda_1 \neq \lambda_2, \end{cases} \\ \int^\theta \frac{\sin^2 \tilde{\theta}}{\lambda_1 \cos^2 \tilde{\theta} + \lambda_2 \sin^2 \tilde{\theta}} d\tilde{\theta} &= \begin{cases} \frac{\theta - \sin \theta \cos \theta}{2\lambda_1}, & \lambda_1 = \lambda_2, \\ \frac{\sqrt{\lambda_1/\lambda_2}}{\lambda_1 - \lambda_2} \left( \arctan \left( \tan \theta \sqrt{\lambda_1/\lambda_2} \right) + \pi \left[ \frac{\theta}{\pi} - \frac{1}{2} \right] \right) - \frac{\theta}{\lambda_1 - \lambda_2}, & \lambda_1 \neq \lambda_2, \end{cases} \\ \int^\theta \frac{\cos^2 \tilde{\theta}}{\lambda_1 \cos^2 \tilde{\theta} + \lambda_2 \sin^2 \tilde{\theta}} d\tilde{\theta} &= \begin{cases} \frac{\theta + \sin \theta \cos \theta}{2\lambda_1}, & \lambda_1 = \lambda_2, \\ \frac{\sqrt{\lambda_2/\lambda_1}}{\lambda_2 - \lambda_1} \left( \arctan \left( \tan \theta \sqrt{\lambda_2/\lambda_1} \right) + \pi \left[ \frac{\theta}{\pi} - \frac{1}{2} \right] \right) - \frac{\theta}{\lambda_1 - \lambda_2}, & \lambda_1 \neq \lambda_2, \end{cases} \\ \int^\theta \frac{\sin \tilde{\theta}}{\sqrt{\lambda_1 \cos^2 \tilde{\theta} + \lambda_2 \sin^2 \tilde{\theta}}} d\tilde{\theta} &= \begin{cases} -\frac{\cos \theta}{\sqrt{\lambda_1}}, & \lambda_1 = \lambda_2, \\ -\frac{\ln \left( \frac{\lambda_2}{\sqrt{\lambda_1 - \lambda_2} |\cos \theta| + \sqrt{(\lambda_1 - \lambda_2) \cos^2 \theta + \lambda_2}} \right)}{\sqrt{\lambda_1 - \lambda_2}}, & \cos \theta < 0, \lambda_1 \neq \lambda_2, \\ -\frac{\ln \left( \sqrt{\lambda_1 - \lambda_2} \cos \theta + \sqrt{(\lambda_1 - \lambda_2) \cos^2 \theta + \lambda_2} \right)}{\sqrt{\lambda_1 - \lambda_2}}, & \cos \theta \geq 0, \lambda_1 \neq \lambda_2, \end{cases} \\ \int^\theta \frac{\cos \tilde{\theta}}{\sqrt{\lambda_1 \cos^2 \tilde{\theta} + \lambda_2 \sin^2 \tilde{\theta}}} d\tilde{\theta} &= \begin{cases} \frac{\sin \theta}{\sqrt{\lambda_1}}, & \lambda_1 = \lambda_2, \\ -\frac{\left( \arctan \left( \frac{\lambda_1}{2 \sin \theta} + \frac{(\lambda_2 - \lambda_1) \sin \theta}{\sqrt{\lambda_1 - \lambda_2} \sqrt{\lambda_1 \cos^2 \theta + \lambda_2 \sin^2 \theta}} \right) + \pi \left[ \frac{\theta}{\pi} \right] - 2\pi \left[ \frac{\theta}{2\pi} \right] \right)}{2\sqrt{\lambda_1 - \lambda_2}}, & \lambda_1 \neq \lambda_2, \end{cases} \end{aligned}$$

where  $\lambda_1$  and  $\lambda_2$  are the eigenvalues of  $\mathbf{G}^{-1}$ , satisfying

$$\tilde{\mathbf{G}}^{-1} = \begin{pmatrix} \tilde{g}^{11} & \tilde{g}^{12} \\ \tilde{g}^{21} & \tilde{g}^{22} \end{pmatrix} = \tilde{\mathbf{Q}}^T \begin{pmatrix} \lambda_1 & 0 \\ 0 & \lambda_2 \end{pmatrix} \tilde{\mathbf{Q}}, \quad \tilde{\mathbf{Q}} = \begin{pmatrix} \cos \phi_G & -\sin \phi_G \\ \sin \phi_G & \cos \phi_G \end{pmatrix}, \quad \lambda_1 \geq \lambda_2.$$

### 3.3.3 Treatment of subregion boundaries

The transformations from the reference region  $\tilde{\Omega}$  to six faces of the cubed sphere are different from each other and not continuous across the edges of the cubed sphere. It means that the approximate local evolution operators corresponding to different cubed sphere faces will give different states (3.20)-(3.22) so that the conservation of the numerical flux cannot be ensured on the edges of the cubed-sphere face. Thus it is necessary to propose some special treatments in order to get the conservation of the numerical flux on the edges of the cubed-sphere face.

To avoid such flaw, around the edges of the cubed-sphere face, the SWEs in the LAT/LON coordinates are linearized on the edges of cubed-sphere face instead of linearizing the

SWEs in the reference coordinates and then its approximate local evolution operator is derived and used to replace that defined by (3.20)-(3.22). To accomplish such task, the SWEs (2.5) are reformulated as follows

$$\frac{\partial \mathbf{V}_s}{\partial t} + \mathbf{A}_s^1(\mathbf{V}_s, \boldsymbol{\xi}) \frac{\partial \mathbf{V}_s}{\partial \xi} + \mathbf{A}_s^2(\mathbf{V}_s, \boldsymbol{\xi}) \frac{\partial \mathbf{V}_s}{\partial \eta} = \mathbf{S}_s, \quad (3.23)$$

where  $\mathbf{V}_s = (h, u_s, v_s \cos \eta)^T$ ,  $\boldsymbol{\xi} = (\xi, \eta)$ ,  $\mathbf{S}_s = (0, S_s^{(1)}, S_s^{(2)})^T$ ,

$$\mathbf{A}_s^1(\mathbf{V}_s, \boldsymbol{\xi}) = \frac{1}{R \cos \eta} \begin{pmatrix} u_s & h & 0 \\ gg_s^{11} & u_s & 0 \\ gg_s^{12} & 0 & u_s \end{pmatrix}, \quad \mathbf{A}_s^2(\mathbf{V}_s, \boldsymbol{\xi}) = \frac{1}{R \cos \eta} \begin{pmatrix} v_s \cos \eta & 0 & h \\ gg_s^{12} & v_s \cos \eta & 0 \\ gg_s^{22} & 0 & v_s \cos \eta \end{pmatrix},$$

$$S_s^{(1)} = \frac{1}{R \cos \eta} (f v_s \cos \eta + u_s v_s \sin \eta - gg_s^{11} b_\xi),$$

$$S_s^{(2)} = -\frac{1}{R \cos \eta} (f u_s \cos \eta + u_s^2 \sin \eta + gg_s^{22} b_\eta + v_s^2 \cos \eta \sin \eta),$$

and

$$\mathbf{G}_s^{-1} = \begin{pmatrix} g_s^{11} & g_s^{12} \\ g_s^{12} & g_s^{22} \end{pmatrix} = \begin{pmatrix} 1 & 0 \\ 0 & \cos^2 \eta \end{pmatrix}.$$

Similarly, if taking  $\tilde{\boldsymbol{\xi}} = (\tilde{\xi}, \tilde{\eta})$  and  $\tilde{\mathbf{V}}_s = [\tilde{h}_s, \tilde{u}_s, \tilde{v}_s \cos \tilde{\eta}]^T$  and as a reference point and state of  $\mathbf{V}_s(\xi, \eta, t)$ , then the system (3.23) may be linearized as follows

$$\frac{\partial \mathbf{V}_s}{\partial t} + \mathbf{A}_s^1(\tilde{\mathbf{V}}_s, \tilde{\boldsymbol{\xi}}) \frac{\partial \mathbf{V}_s}{\partial \xi} + \mathbf{A}_s^2(\tilde{\mathbf{V}}_s, \tilde{\boldsymbol{\xi}}) \frac{\partial \mathbf{V}_s}{\partial \eta} = \mathbf{S}_s, \quad (3.24)$$

whose form is similar to the previous linearized system (2.11) in the reference coordinates. On the other hand, the derivation of the approximate local evolution operator of (2.11) does not require the concrete form of  $\mathbf{G}^{-1}$ ,  $\mathbf{V}$  and  $\mathbf{x}$ . Hence the approximate local evolution operator of the system (3.24) may be derived in parallel by replacing  $\mathbf{G}^{-1}$ ,  $\mathbf{V}$ , and  $\mathbf{x}$  with  $\mathbf{G}_s^{-1}$ ,  $\mathbf{V}_s$ , and  $\boldsymbol{\xi}$  in Sections 2.3, 3.3.1 and 3.3.2, respectively. However, a special attention should be paid to calculate the intersection points between the bottom of the bicharacteristic cone past the point on the edges of the cubed sphere face and the cell edges in the  $(\xi, \eta)$  plane. The readers are referred to Appendix B for the detailed discussion. Because the cell edges in the LAT/LON plane are not straight in general, calculation of those intersection points is different from those in the  $(x, y)$  plane discussed in Appendix A.

**Remark 3.3** *Because the edges of the cubed sphere face do not pass through the spherical pole, the pole singularity in the LAT/LON coordinates may be gotten around.*

At the end of this section, the conservation of the numerical flux of the RKDLEG method on the edges of cubed sphere faces. Let  $\mathcal{L}$  and  $\mathcal{L}_s$  denote the edge of the cubed sphere

face in the  $(x, y)$  and LAT/LON planes, respectively, and  $\mathbf{n}$  and  $\mathbf{n}_s$  be their outward unit normal vectors.

**Theorem 3.2** *The numerical flux of the RKDLEG method in the LAT/LON plane*

$$\int_{\mathcal{L}} \begin{pmatrix} \mathbf{I} & 0 \\ 0 & \mathbf{A} \end{pmatrix} \mathbf{F}(\mathcal{E}_{h,0} \mathbf{V}_h(t)) \cdot \mathbf{n} dl,$$

does not depend on the transformation from  $(x, y)$  to  $(\xi, \eta)$ , but relies on the height  $h$  and velocity  $(u_s, v_s)$  in the LAT/LON plane.

**Proof** Due to the transformation between the reference coordinates  $(x, y)$  and LAT/LON coordinates  $(\xi, \eta)$ , one has  $\mathbf{A}^T \cdot \mathbf{n}_s = \mathbf{n}$ . Using (2.2), (2.3), and

$$\mathbf{F}(\mathbf{U}) = \begin{pmatrix} \Lambda hu & \Lambda hv \\ \Lambda (hu^2 + \frac{1}{2}gg^{11}h^2) & \Lambda (huv + \frac{1}{2}gg^{12}h^2) \\ \Lambda (huv + \frac{1}{2}gg^{12}h^2) & \Lambda (hu^2 + \frac{1}{2}gg^{22}h^2) \end{pmatrix},$$

gives

$$\begin{aligned} \int_{\mathcal{L}} \begin{pmatrix} \mathbf{I} & 0 \\ 0 & \mathbf{A} \end{pmatrix} \mathbf{F}(\mathbf{U}) \cdot \mathbf{n} dl &= \int_{\mathcal{L}} \begin{pmatrix} \mathbf{I} & 0 \\ 0 & \mathbf{A} \end{pmatrix} \mathbf{F}(\mathbf{U}) \mathbf{A}^T \mathbf{n}_s dl \\ &= \int_{\mathcal{L}} \begin{pmatrix} \mathbf{I} & 0 \\ 0 & \mathbf{A} \end{pmatrix} \begin{pmatrix} \Lambda hu & \Lambda hv \\ \Lambda (hu^2 + \frac{1}{2}gg^{11}h^2) & \Lambda (huv + \frac{1}{2}gg^{12}h^2) \\ \Lambda (huv + \frac{1}{2}gg^{12}h^2) & \Lambda (hv^2 + \frac{1}{2}gg^{22}h^2) \end{pmatrix} \mathbf{A}^T \mathbf{n}_s dl \\ &= \int_{\mathcal{L}} \begin{pmatrix} \Lambda hu_s & \Lambda hv_s \\ \Lambda ((hu_s^2 + \frac{1}{2}gh^2) & \Lambda (hu_s v_s + \frac{1}{2}gh^2) \\ \Lambda ((hu_s v_s + \frac{1}{2}gh^2) & \Lambda (hv_s^2 + \frac{1}{2}gh^2) \end{pmatrix} \mathbf{n}_s dl \\ &= \int_{\mathcal{L}_s} \begin{pmatrix} hu_s & hv_s \\ (hu_s^2 + \frac{1}{2}gh^2) & (hu_s v_s + \frac{1}{2}gh^2) \\ (hu_s v_s + \frac{1}{2}gh^2) & (hv_s^2 + \frac{1}{2}gh^2) \end{pmatrix} \mathbf{n}_s dl_s, \end{aligned}$$

in which the states are evolved through the linearized SWEs in the LAT/LON coordinates. The proof is completed. ■

## 4 Numerical experiments

This section will apply the proposed RKDLEG methods to several benchmark problems [49] for the SWEs on the sphere to demonstrate the accuracy and performance of the present methods. In our computations, the CFL number  $C_{cfl}$  is taken as 0.25, 0.15, and 0.1 for the  $\mathbb{P}^1$ -,  $\mathbb{P}^2$ -, and  $\mathbb{P}^3$ -based RKDLEG methods, respectively, and the region  $\{(x, y) \mid x, y \in \tilde{\Omega}\}$  in Fig. 2.1 (b) is divided into  $N \times N$  uniform cells, that is, the sphere surface is partitioned into  $6(N \times N)$  cells.

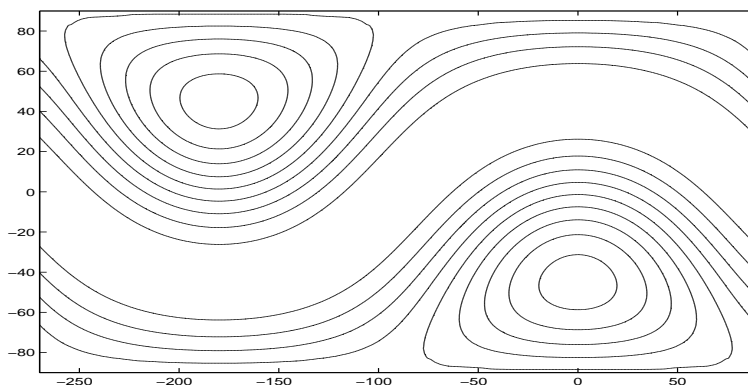


Fig. 4.1. Example 4.1: The height  $h(\xi, \eta, t)$  at  $t = 3$  days obtained by using the  $\mathbb{P}^3$ -based RKDLEG method with  $N = 64$ . Contour lines are equally spaced from 1150 m to 2950 m with a stepsize of 200 m.

**Example 4.1 (Steady state zonal geostrophic flow)** This example is Williamson’s test case 2 [49], in which the initial height and divergence-free velocity vector in the LAT/LON coordinates  $(\xi, \eta)$  are given by

$$\begin{aligned} h(\xi, \eta, 0) &= h_0 - g^{-1} \left( R\Omega u_0 + \frac{u_0^2}{2} \right) (-\cos \xi \cos \eta \sin \alpha + \sin \eta \cos \alpha)^2, \\ u_s(\xi, \eta, 0) &= u_0 (\cos \eta \cos \alpha + \cos \xi \sin \eta \sin \alpha), \quad v_s(\xi, \eta, 0) = -u_0 \sin \xi \sin \alpha, \end{aligned} \quad (4.1)$$

where  $h_0 = 2.94 \times 10^4$  m,  $u_0 = \frac{2\pi R}{12}$  day $^{-1}$ , and  $\alpha$  denotes the angle between the rotational and polar axes of the sphere (or the Earth) and may be chosen as  $\alpha = 0$  or  $\frac{\pi}{4}$  or  $\frac{\pi}{2}$ . The Coriolis force is calculated as

$$f = 2\Omega (-\cos \xi \cos \eta \sin \alpha + \sin \eta \cos \alpha).$$

The exact solution to this problem describes a steady state flow, where the physical variables  $h$ ,  $u_s$ , and  $v_s$  at any time are the same as the initial. Fig. 4.1 shows the height  $h(\xi, \eta, t)$  at  $t = 3$  days obtained by the  $\mathbb{P}^3$ -based RKDLEG method with  $N = 64$ . Tables 4.1-4.3 list the relative errors in the height  $h$  at  $t = 3$  days and corresponding convergence rates of the  $\mathbb{P}^1$ -,  $\mathbb{P}^2$ -, and  $\mathbb{P}^3$ -based RKDLEG methods, where the  $l_1$ -,  $l_2$ -, and  $l_\infty$ -errors



are respectively measured by [49]

$$\frac{\int_S |h_h - h| ds}{\int_S |h| ds}, \quad \frac{\left[ \int_S (h_h - h)^2 ds \right]^{\frac{1}{2}}}{\left( \int_S h^2 ds \right)^{\frac{1}{2}}}, \quad \frac{\max\{|h_h - h|\}}{\max\{|h|\}}.$$

Here  $S$  is the whole sphere surface,  $h_h$ , and  $h$  denote the numerical and exact heights, respectively, and those integrations are calculated by using the Gauss-Lobatto quadrature rule. Those data show that the  $\mathbb{P}^K$ -based RKDLEG method is of  $(K + 1)$ th order of convergence,  $k = 1, 2, 3$ . Fig. 4.2 displays the time evolutions of the log of relative errors to base 10 in  $h, u, v$  obtained by the  $\mathbb{P}^3$ -based RKDLEG method with  $N = 64$ .

Fig. 4.3 plots the relative conservation errors of the  $\mathbb{P}^3$ -based RKDLEG method with  $N = 64$  in the total mass, energy, and potential enstrophy [48], defined by

$$\mathcal{M}(t) = \int_S h ds, \quad \mathcal{E}(t) = \int_S \left( \frac{1}{2} h (u_s^2 + v_s^2) + \frac{1}{2} g \left( (h + b)^2 - b^2 \right) \right) ds, \quad \mathcal{P}(t) = \int_S \frac{(\varsigma + f)^2}{2h} ds,$$

where  $\varsigma = \frac{1}{\Lambda} \left( \frac{\partial \hat{v}}{\partial x} - \frac{\partial \hat{u}}{\partial y} \right)$  denotes the relative vorticity, and  $(\hat{u}, \hat{v})$  are given in Eq. (2.2). The results show that the error of total mass  $(\mathcal{M}(t) - \mathcal{M}(0))/\mathcal{M}(0)$  is very close to the machine (or round-off) precision, the error of total energy is very small and oscillatory decreasing, while the error of potential enstrophy is also small but monotonically increasing.

Table 4.1

Example 4.1: The relative errors in the height  $h$  at  $t = 3$  days and convergence rates by  $\mathbb{P}^1$ -based RKDLEG method.

$N$	$l_1$ -error	order	$l_2$ -error	order	$l_\infty$ -error	order
16	1.23e-03	–	1.56e-03	–	1.07e-02	–
32	2.67e-04	2.2019	3.54e-04	2.1392	3.05e-03	1.8046
64	6.09e-05	2.1326	8.42e-05	2.0707	1.07e-03	1.8931

Table 4.2

Same as Table 4.1 except for  $\mathbb{P}^2$ -based RKDLEG method.

$N$	$l_1$ -error	order	$l_2$ -error	order	$l_\infty$ -error	order
16	2.83e-05	–	4.28e-05	–	4.11e-04	–
32	3.47e-06	3.0260	5.32e-06	3.0059	5.64e-05	2.8648
64	4.31e-07	3.0070	6.65e-07	3.0018	8.24e-06	2.7759

Table 4.3

Same as Table 4.1 except for  $\mathbb{P}^3$ -based RKDLEG method.

$N$	$l_1$ -error	order	$l_2$ -error	order	$l_\infty$ -error	order
16	9.82e-07	–	1.61e-06	–	4.68e-05	–
32	6.04e-08	4.0222	9.99e-08	4.0060	3.83e-06	3.6088
64	3.82e-09	3.9843	6.55e-09	3.9318	7.07e-07	2.4384

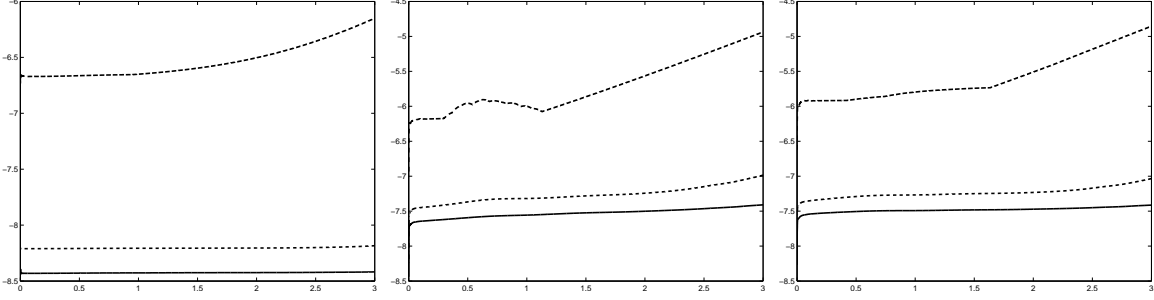


Fig. 4.2. Example 4.1. The time evolution of the log of relative errors to base 10 in  $h$ ,  $u$ , and  $v$  (from left to right) obtained by using the  $\mathbb{P}^3$ -based RKDLEG method with  $N = 64$ , where the solid, dashed, and dotted lines denote the  $l_1$ -,  $l_2$ -, and  $l_\infty$ -errors, respectively.

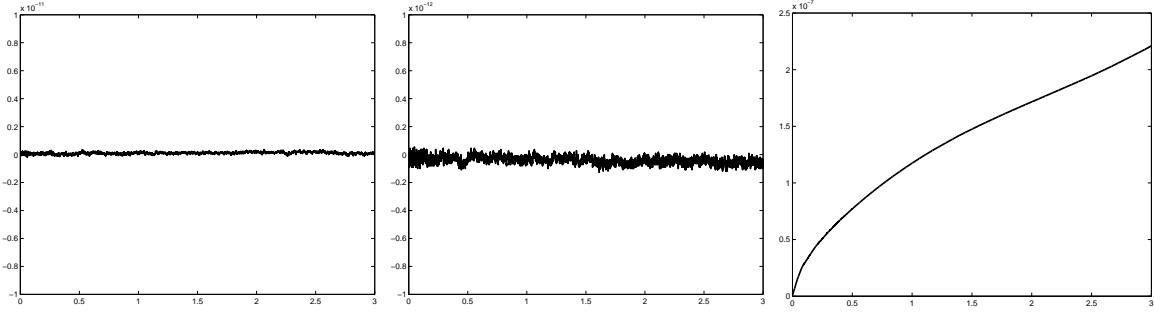


Fig. 4.3. Example 4.1: The time evolution of the relative conservation errors of total mass, energy, and potential enstrophy (from left to right) obtained by using the  $\mathbb{P}^3$ -based RKDLEG method with  $N = 64$ .

**Example 4.2 (Time dependent zonal flow)** This example is about a time dependent zonal flow and challenging to evaluate the numerical methods, see [6,36]. The analytical solutions to this problem [20] can be given by

$$\begin{aligned}
 h(\xi, \eta, t) &= -\frac{1}{2g} [u_0 \sin \alpha \cos \theta (-\cos \xi \cos(\Omega t) + \sin \xi \sin(\Omega t) + \cos \alpha \sin \eta) \\
 &\quad + R\Omega \sin \eta]^2 + \frac{1}{2g} (R\Omega \sin \eta)^2 + g^{-1}k_1 - b(\eta), \\
 u_s(\xi, \eta, t) &= u_0 [\sin \alpha \sin \eta (\cos \xi \cos(\Omega t) - \sin \xi \sin(\Omega t)) + \cos \alpha \cos \eta], \\
 v_s(\xi, \eta, t) &= -u_0 [\sin \alpha (\sin \xi \cos(\Omega t) + \cos \xi \sin(\Omega t))],
 \end{aligned}$$

where  $b(\eta) = \frac{1}{2g} (R\Omega \sin \eta)^2 + g^{-1}k_2$  is the height of bottom mountain,  $u_0 = \frac{2\pi R}{12} \text{ day}^{-1}$ ,  $k_1 = 133681 \text{ m}$ ,  $k_2 = 0 \text{ m}$ , and  $\alpha$  is taken as  $\frac{\pi}{4}$ . Fig. 4.4 gives the contour plot of height  $h$  at  $t = 5$  days obtained by using the  $\mathbb{P}^2$ -based RKDLEG method with  $N = 64$ .

Fig. 4.5 gives a comparison of the  $\mathbb{P}^1$ -based RKDLEG method to the second-order accurate finite volume LEG (abbr. FVLEG) method. Those error plots show that the errors of the  $\mathbb{P}^1$ -based RKDLEG method grows more slowly and much smaller than the FVLEG method. The relative errors in  $h, u, v$  of the  $\mathbb{P}^2$ -based RKDLEG method shown in Fig. 4.6 is similar to the  $\mathbb{P}^1$ -based RKDLEG method. Fig. 4.7 plots the relative conservation errors in the total mass, energy, and potential enstrophy obtained by the  $\mathbb{P}^2$ -based RKDLEG method with  $N = 64$ . The results show the total mass is numerically conservative, the

total energy is decreasing with an approximate slope of  $-7.2 \times 10^{-11}$ , and the error in the total potential enstrophy is about  $O(10^{-6})$ .

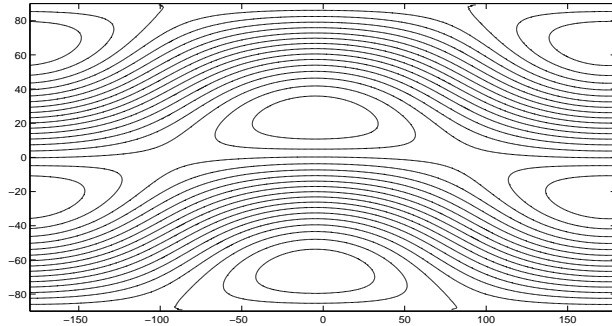


Fig. 4.4. Example 4.2: The height  $h(\xi, \eta, t)$  at  $t = 5$  days obtained by using the  $\mathbb{P}^2$ -based RKDLEG method with  $N = 64$ . Contour lines are equally spaced from 12000 m to 13800 m with a stepsize of 100 m.

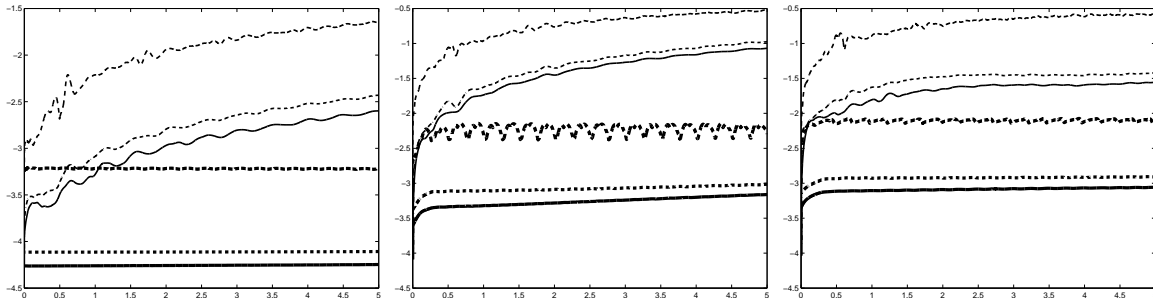


Fig. 4.5. Example 4.2: The time evolution of the log of relative errors to base 10 in  $h$ ,  $u$ , and  $v$  (from left to right) obtained by using the  $\mathbb{P}^1$ -based RKDLEG method (wide lines) and FVLEG method (thin lines) with  $N = 16, 32, 64$  (resp. dashed, dotted, and solid lines), respectively.

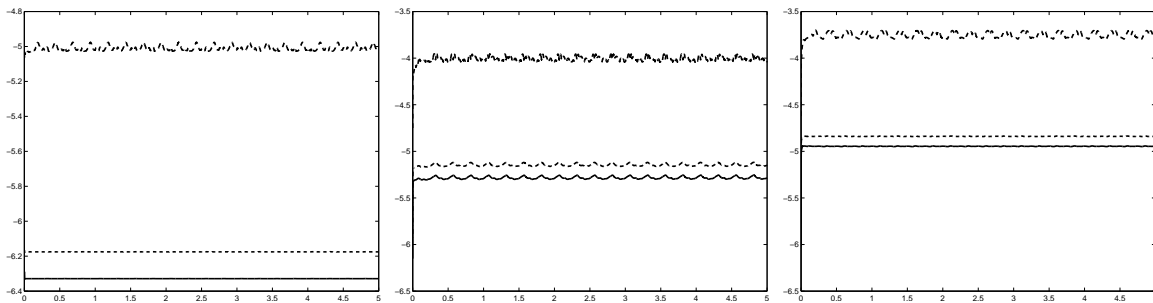


Fig. 4.6. Example 4.2: Same as Fig. 4.2 except for example 4.2 by using  $\mathbb{P}^2$ -based RKDLEG method.

**Example 4.3 (Zonal flow over a bottom mountain)** The third example considers Williamson's test case 5 [49], in which the initial height  $h$  and velocity vector  $(u_s, v_s)$  are given in Eq. (4.1) with  $h_0 = 5960$  m,  $\alpha = 0$ , and  $u_0 = 20$  s $^{-1}$ . The bottom mountain is centered at  $(\xi_c, \eta_c) = \left(-\frac{\pi}{2}, \frac{\pi}{6}\right)$ , and its height is given by

$$b = b_0 \left(1 - \frac{r}{r_0}\right),$$

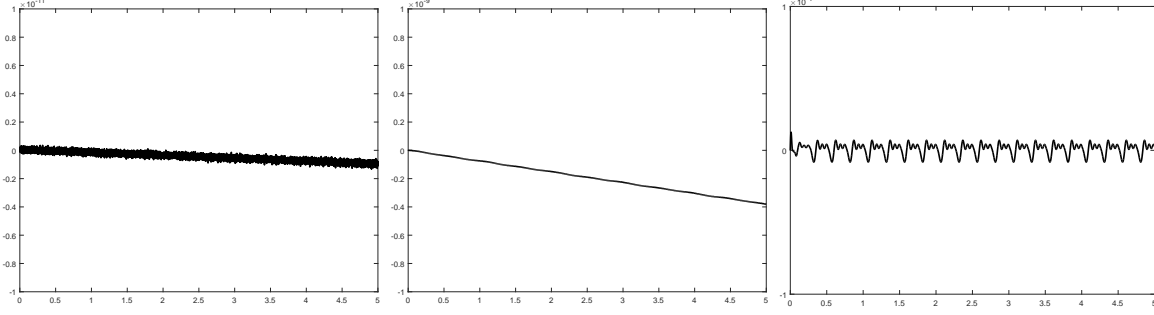


Fig. 4.7. Example 4.2: Same as Fig. 4.3 except for example 4.2 by using  $\mathbb{P}^2$ -based RKDLEG method.

where  $r = \min \left\{ r_0, \sqrt{(\xi - \xi_c)^2 + (\eta - \eta_c)^2} \right\}$ ,  $b_0 = 2000$  m, and  $r_0 = \frac{\pi}{9}$ . Fig. 4.8 shows the contour plots of height  $h$  at  $t = 5, 10$  and  $15$  days obtained by using the  $\mathbb{P}^3$ -based RKDLEG method. Due to the bottom mountain, the flow pattern observed here is unsteady and fully different from that in Fig. 4.1. Comparing those with the reference solution in [16], the present RKDLEG method may calculate the height accurately. Corresponding relative conservation errors in the total mass, total energy and potential enstrophy are given in Fig. 4.9. We see that the total mass is conservative and the errors in the total energy and potential enstrophy are about  $O(10^{-8})$  and  $O(10^{-4})$ , respectively.

**Example 4.4 (Deformational flow)** This example is an extension of the pure advection flow but with deformation introduced in [33] to the SWEs (3.23) by adding two “source” terms

$$-\frac{g}{\cos \eta} \frac{\partial \left( \tanh\left(\frac{\rho}{\gamma} \sin(\xi - \omega t)\right) \right)}{\partial \xi}, \quad -g \frac{\partial \left( \tanh\left(\frac{\rho}{\gamma} \sin(\xi - \omega t)\right) \right)}{\partial \eta} + (f + \omega \sin \eta) R \omega \cos \eta.$$

to the right-hand side of two momentum equations respectively. The initial height  $h$  and velocity vector  $(u_s, v_s)$  are specified by

$$h(\xi, \eta, 0) = R - R \tanh \left( \frac{\rho}{\gamma} \sin \xi \right), \quad u_s(\xi, \eta, 0) = R \omega \cos \eta, \quad v_s(\xi, \eta, 0) = 0,$$

where  $\rho = \rho_0 \cos \eta$ ,  $\rho_0 = 3$ ,  $\gamma = 5$ , and the angular velocity

$$\omega = \begin{cases} \frac{3\sqrt{3}}{2} u_0 \frac{\tanh \rho}{\rho \cosh^2 \rho}, & \rho \neq 0, \\ 0, & \rho = 0, \end{cases}$$

with  $u_0 = \frac{\pi}{6} \text{day}^{-1}$ . The exact height field is taken as

$$h(\xi, \eta, t) = R - R \tanh \left( \frac{\rho}{\gamma} \sin(\xi - \omega t) \right),$$

and shown in Fig. 4.10 for  $t = 6$  and  $12$  days.

Fig. 4.11 gives the heights  $h$  at  $t = 6$  and  $12$  days obtained by using the  $\mathbb{P}^3$ -based RKDLEG method with  $N = 32$ . It is obvious that they are in accordance with those in Fig. 4.10.

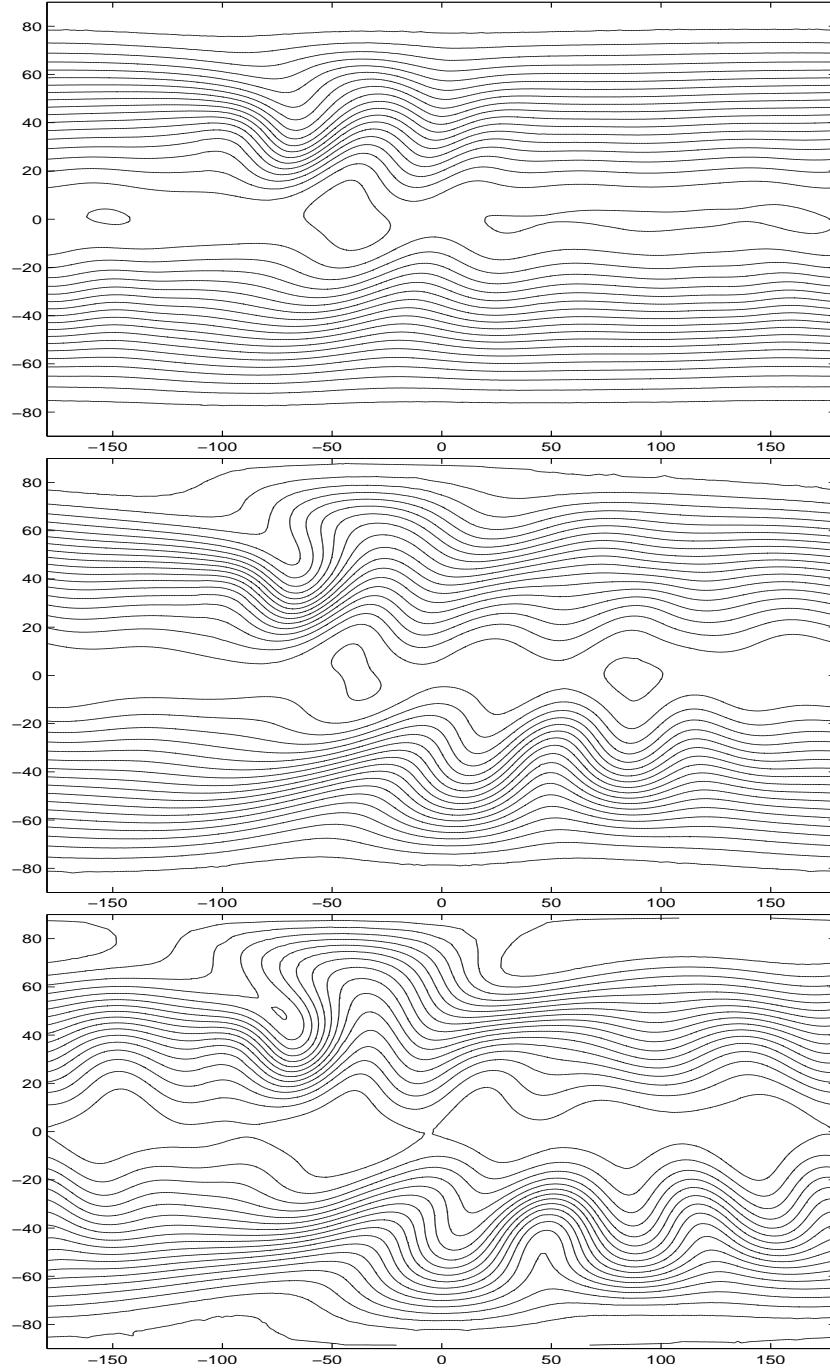


Fig. 4.8. Example 4.3: The heights  $h(\xi, \eta, t)$  at  $t = 5, 10$  and  $15$  days (from top to bottom) obtained by using the  $\mathbb{P}^3$ -based RKDLEG method with  $N = 32$ . Contour lines are equally spaced from  $5050$  m to  $5950$  m with a stepsize of  $50$  m.

Fig. 4.12 gives the numerical results at  $t = 6$  days obtained by using the  $\mathbb{P}^1$ -based RKDLEG method and  $\mathbb{P}^1$ -based RKDG method with Godunov's flux. Comparing them to the exact solution in the left plot of Fig. 4.10, we see that the  $\mathbb{P}^1$ -based RKDG method with Godunov's flux gives an inaccurate solution in this case.

**Example 4.5 (Rossby-Haurwitz wave)** Rossby-Haurwitz waves are steadily propa-

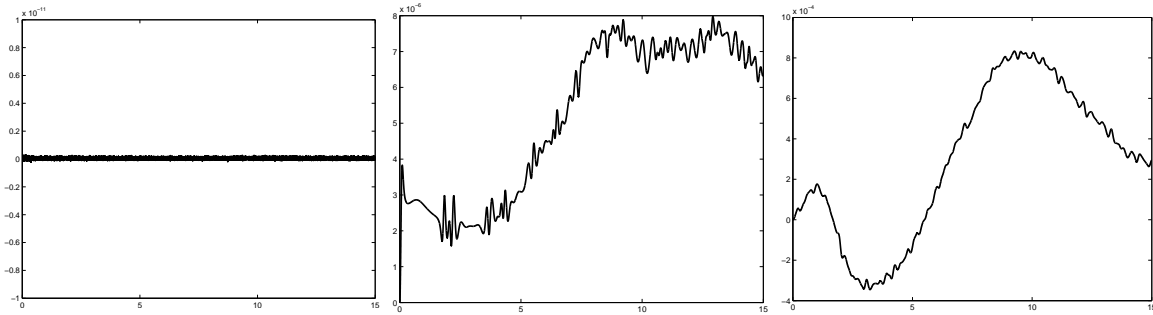


Fig. 4.9. Example 4.3: Same as Fig. 4.3 except for example 4.3 with  $N = 32$ .

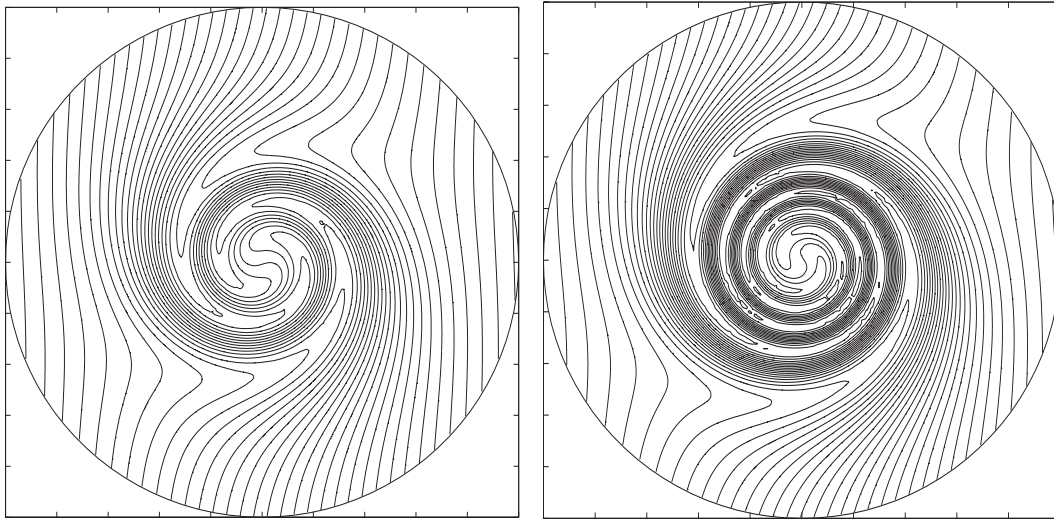


Fig. 4.10. Example 4.4: The exact heights  $h$  at  $t = 6, 12$  days (from left to right), which are viewed from the North pole of the Earth. Contour lines are equally spaced from 300 m to 960 m with a stepsize of 20 m.

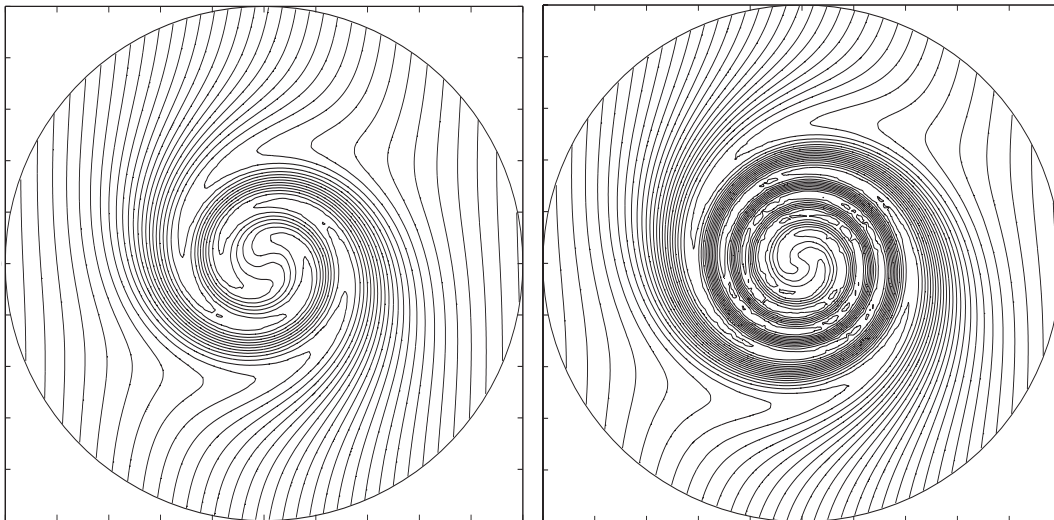


Fig. 4.11. Same as Fig. 4.10 except for the numerical heights  $h$  obtained by using  $\mathbb{P}^3$ -based RKDLEG method with  $N = 32$ .



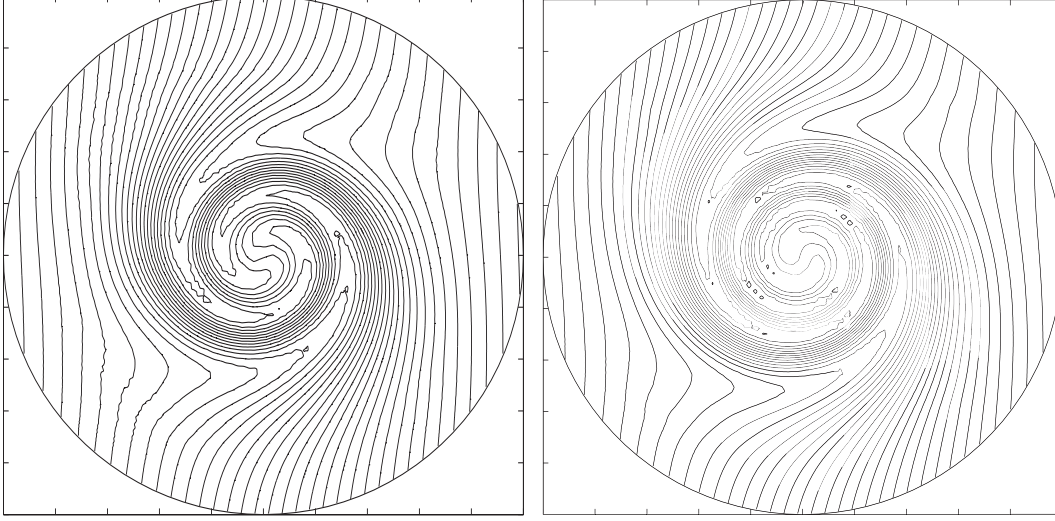


Fig. 4.12. Same as the left plot in Fig. 4.11 except for the  $\mathbb{P}^1$ -based RKDLEG method (left) and RKDG method with Godunov's flux (right).

gating solutions of the fully nonlinear non-divergent barotropic vorticity equation on a sphere and have been used to test shallow water numerical models, see the 6th case of the standard shallow-water test provided by Williamson et al. [49]. Rossby-Haurwitz waves with zonal wave-numbers less than or equal to 5 are commonly believed to be stable, otherwise unstable.

The initial height and divergence-free velocity vector are specified as follows

$$\begin{aligned} h(\xi, \eta, 0) &= h_0 + g^{-1} R^2 (A(\eta) + B(\eta) \cos(r\xi) + C(\eta) \cos(2r\xi)), \\ u_s(\xi, \eta, 0) &= RK \cos \eta + RK \cos^{r-1} \eta (r \sin^2 \eta - \cos^2 \eta) \cos(r\xi), \\ v_s(\xi, \eta, 0) &= -RK r \cos^{r-1} \eta \sin \eta \sin(r\xi), \end{aligned}$$

where

$$\begin{aligned} A(\eta) &= \frac{K}{2} (2\Omega + K) \cos^2 \eta + \frac{1}{4} K^2 \cos^{2r} \eta \left[ (r+1) \cos^2 \eta + (2r^2 - r - 2) - \frac{2r^2}{\cos^2 \eta} \right], \\ B(\eta) &= \frac{2(\Omega + K)K}{(r+1)(r+2)} \cos^r \eta \left[ (r^2 + 2r + 2) - (r+1)^2 \cos^2 \eta \right], \\ C(\eta) &= \frac{1}{4} K^2 \cos^{2r} \eta \left[ (r+1) \cos^2 \eta - (r+2) \right], \end{aligned}$$

with  $K = 7.848 \times 10^{-6} \text{ s}^{-1}$ , the zonal wave number  $r = 4$ , and  $h_0 = 8000 \text{ m}$ .

Fig. 4.13 displays the heights at  $t = 7$  and 14 days obtained by using the  $\mathbb{P}^3$ -based RKDLEG method with  $N = 48$ . Those results agree well with the widely accepted reference solutions [16], the wave propagates steadily eastward, and superposed on this steady propagation are small vacillations in the wave structure. Fig. 4.3 gives the time evolution of the relative conservation errors of total mass, total energy and potential enstrophy. It is obvious that the total mass is conservative and the error in the total energy is about



$O(10^{-7})$ , but the error in the total potential enstrophy is slightly big and its order of magnitude is  $-2$ .

Figs. 4.15 and 4.16 also give the solutions at  $t = 7$  and 14 days obtained respectively by using the  $\mathbb{P}^1$ -based RKDLEG method and  $\mathbb{P}^1$ -based RKDG method with Godunov's flux with  $N = 48$ . Comparing them, it is not difficult to see that the RKDLEG method may get the solutions more similar to the reference solutions [16] than the RKDG method with Godunov's flux.

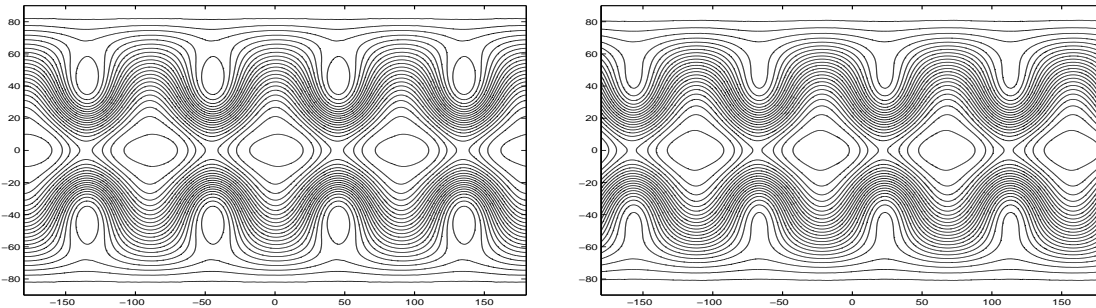


Fig. 4.13. Example 4.5: The heights at  $t = 7$  (left) and 14 days (right) obtained by using  $\mathbb{P}^3$ -based RKDLEG method with  $N = 48$ . Contour lines are equally spaced from 8100 m to 11000 m with a stepsize of 100 m.

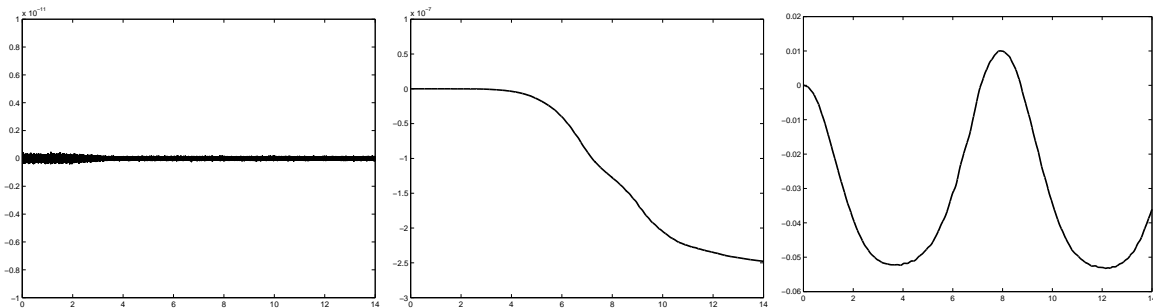


Fig. 4.14. Example 4.5. Same as Fig. 4.3 except for example 4.5 with  $N = 48$ .

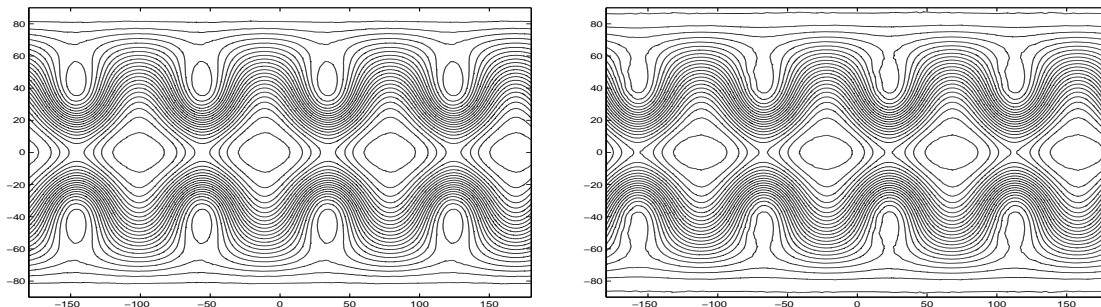


Fig. 4.15. Same as Fig. 4.13 except for the  $\mathbb{P}^1$ -based RKDLEG method.

**Example 4.6 (Cross-polar flow)** It is first proposed in [31]. Initially, there are a low and high patterns which are symmetrically located at the left and right hand sides of the pole, respectively, when it is viewed from above. The low or high pattern rotates in clockwise direction around the pole [35].

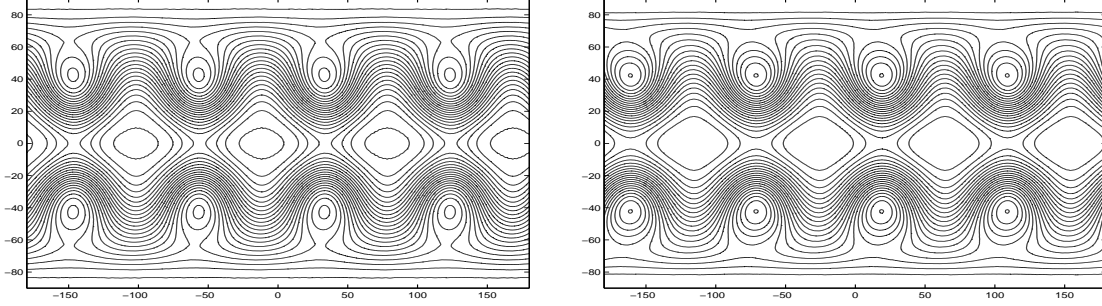


Fig. 4.16. Same as Fig. 4.13 except for the  $\mathbb{P}^1$ -based RKDG method with Godunov's flux.

The initial height and velocity vector are taken as

$$\begin{aligned} h(\xi, \eta, 0) &= h_0 - 2g^{-1}R\omega u_0 \sin^3 \eta \cos \eta \sin \xi, \\ u_s(\xi, \eta, 0) &= -u_0 \sin \xi \sin \eta (4 \cos^2 \eta - 1), \\ v_s(\xi, \eta, 0) &= u_0 \sin^2 \eta \cos \xi, \end{aligned}$$

where  $h_0 = 5.768 \times 10^4 g^{-1}$  m and  $u_0 = 20$  m/s. It means that the initial cross-polar flow is of strength  $u_0$ , and both wind components were zero at the equator.

Fig. 4.17 shows the solutions  $(h, u_s, v_s)$  at  $t = 10$  days obtained by using the  $\mathbb{P}^3$ -based RKDLEG method with  $N = 54$ , where the contour lines of  $h$  are equally spaced from 5350 m to 6330 m with an interval of 80 m, while the contour lines of  $u_s$  and  $v_s$  are taken from  $-21$  m/s to 21 m/s and from  $-13$  m/s to 13 m/s with a stepsize of 2 m/s, respectively. Our results are comparable to those given in [11,35]. The conservation of total mass, energy and potential enstrophy may be demonstrated via the relative conservation error plots given in Fig. 4.18. The errors in the total energy and potential enstrophy are about  $O(10^{-13})$  and  $O(10^{-3})$  respectively.

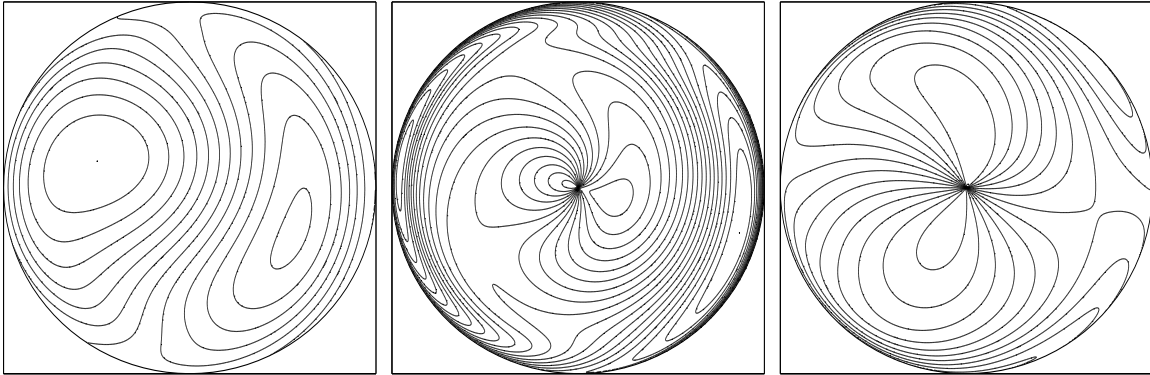


Fig. 4.17. Example 4.6: The solutions  $h$ ,  $u_s$ , and  $v_s$  (from left to right) at  $t = 10$  days obtained by using  $\mathbb{P}^3$ -based RKDLEG method with  $N = 54$ , which are viewed from the North pole.

**Example 4.7 (Unstable barotropic jet flow)** This unstable barotropic jet flow introduced in [10] is similar to Williamson's test 2, but more difficult and challenging for the numerical methods due to the unstable wave structure within a more narrow zonal region and the dynamic balance in the solutions. Specially, it has a great challenge to the numerical methods on the cubed-sphere grid in Fig. 2.1 (a)-(c), see [41], because the jet flow

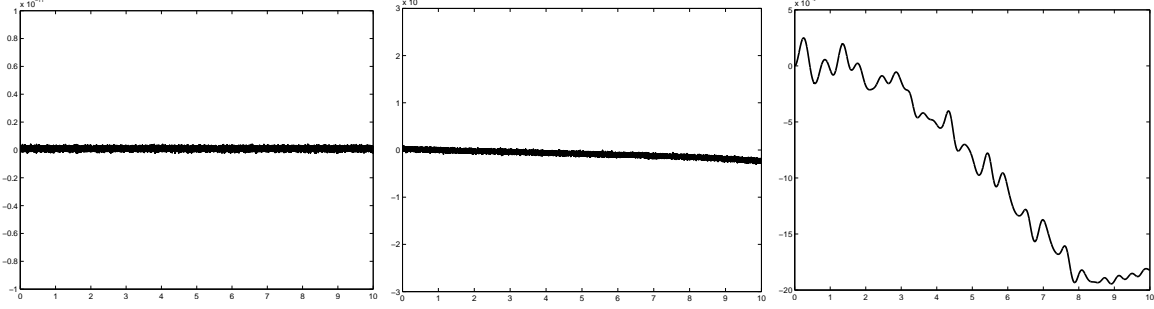


Fig. 4.18. Example 4.6: Same as Fig. 4.3 except for example 4.6 with  $N = 54$ .

is driven by a relatively mild perturbation and then passes over the cubed-sphere edges several times in a long time range.

Initially, the zonal velocity fields are chosen as follows

$$u_s(\xi, \eta, 0) = \begin{cases} u_{\max} e_n^{-1} \exp\left[\frac{1}{(\eta-\eta_0)(\eta-\eta_1)}\right], & \text{if } \eta_0 < \eta < \eta_1, \\ 0, & \text{otherwise,} \end{cases}$$

$$v_s(\xi, \eta, 0) = 0,$$

while the balanced height  $h$  is calculated by the following balance equation

$$h(\xi, \eta, 0) = h_0 - g^{-1} \int_{-\frac{\pi}{2}}^{\eta} R u_s(\eta') \left[ f + \frac{\tan \eta'}{R} u_s(\eta') \right] d\eta',$$

where  $h_0 = 1000$  m,  $u_{\max} = 80$  m/s,  $\eta_0 = \frac{\pi}{7}$ ,  $\eta_1 = \frac{\pi}{2} - \eta_0$ , and  $e_n = \exp\left(-\frac{4}{(\eta_1 - \eta_0)^2}\right)$ . In order to initiate the instability, an initial perturbation

$$h'(\xi, \eta) = \hat{h} \cos(\eta) \exp\left[-\left(\frac{\xi}{\alpha}\right)^2 - \left(\frac{\eta_2 - \eta}{\beta}\right)^2\right],$$

is added to the above balanced height  $h(\xi, \eta, 0)$ , where  $\hat{h} = 120$  m,  $\alpha = \frac{1}{3}$ ,  $\beta = \frac{1}{15}$ , and  $\eta_2 = \frac{\pi}{4}$ . It implies that the initial height  $h$  has a large gradient near the cubed-sphere edges in Fig. 2.1 (a)-(c), and the initial perturbation is located on the edge shared by the subregions  $P_1$  and  $P_5$  in Fig. 2.1 (a).

Fig. 4.19 compares the relative vorticities  $\zeta$  at  $t = 6$  days obtained by using  $\mathbb{P}^3$ -based RKDLEG method,  $\mathbb{P}^3$ -based RKDG method with Godunov's flux, and FVLEG method with fifth-order accurate weighted essentially non-oscillatory (WENO5) reconstruction with  $N = 32$ . It is obvious that the RKDG method with Godunov's flux is influenced by 4-wave errors within the longitude interval  $[-260, -120]$ , and the FVLEG method with WENO5 reconstruction can not give the correct result in comparison to the reference solution in [10] due to the fast growing error as shown in Fig. 4.5. Fig. 4.20 gives the relative conservation errors at  $t = 6$  days in the total mass, total energy and potential enstrophy obtained by using the  $\mathbb{P}^3$ -based RKDLEG method with  $N = 32$ . It is seen that the total mass is conservative, and other errors are about  $O(10^{-6})$  and  $O(10^{-3})$ ,

respectively. Fig. 4.21 further investigates the convergence of the  $\mathbb{P}^3$ -based RKDLEG method, where the relative vorticities are obtained on the finer grids of  $N = 64, 96,$  and  $128,$  respectively. Those results look very similar to the reference solution in [10] except for very little oscillation.

## 5 Conclusions

The paper developed arbitrary high order accurate Runge-Kutta discontinuous local evolution Galerkin (RKDLEG) methods on the cubed-sphere grid for the shallow water equations SWEs. The exact and approximate evolution operators of the locally linearized SWEs in the reference coordinates were first derived based on the theory of bicharacteristics, then the approximate local evolution operator was combined with the Runge-Kutta discontinuous Galerkin (RKDG) methods for the SWEs in spherical geometry. In other words, the proposed RKDLEG methods were built on genuinely multi-dimensional approximate local evolution operator of the locally linearized SWEs in the spherical geometry by considering all bicharacteristic directions, instead of the dimensional splitting method or one-dimensional Riemann solver in the direction normal to the cell interface. A special treatment on the edges of the cubed sphere face was given, where the approximate local evolution operator of the SWEs in the LAT/LON coordinates was replaced with that of the SWEs in the reference coordinates in order to ensure the conservation of numerical flux there. Several benchmark problems were numerically solved to check the accuracy and performance of our RKDLEG methods, in comparison to the RKDG method with Godunov's flux etc. The results showed that in comparison to the RKDG method with Godunov's flux and FVLEG method, the proposed RKDLEG methods were competitive to solve those standard tests of Williamson et al. in terms of accuracy, good multi-dimensional behavior, and long time simulation.

## Acknowledgements

This work was partially supported by the National Natural Science Foundation of China (Nos. 91330205 & 11421101).

## Appendix A

This appendix presents the detailed procedure to evaluate  $\{\theta_i, i = 1, 2, \dots, \hat{N}\}$  in the definition of approximate evolution operator  $\mathcal{E}_h(\tau)$  or  $\mathcal{E}_{h,0}$  in Section 3.3.1 or 3.3.2.

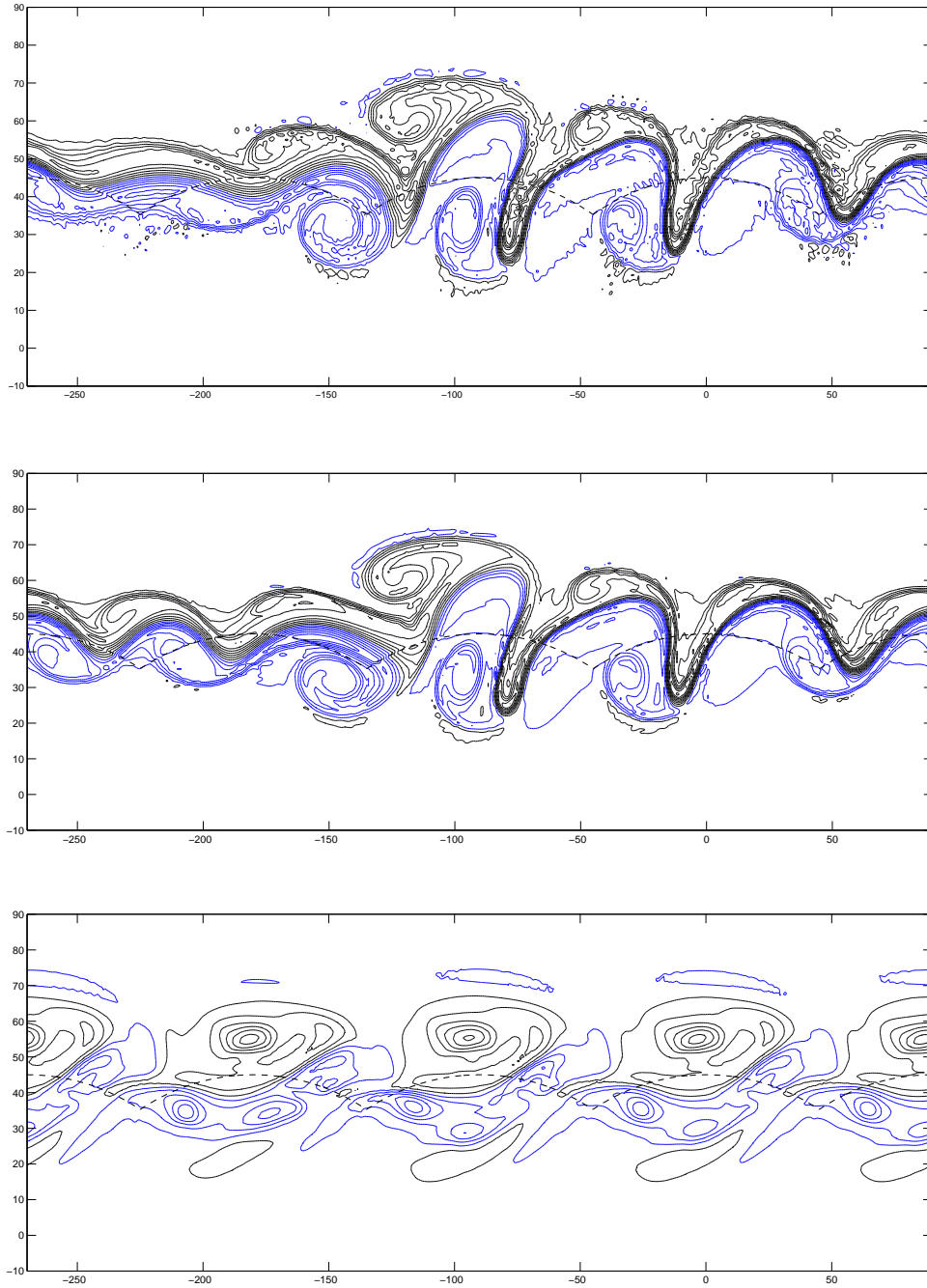


Fig. 4.19. Example 4.7: Relative vorticities at  $t = 6$  days obtained by using by  $\mathbb{P}^3$ -based RKLEG method,  $\mathbb{P}^3$ -based RKDG method with Godunov's flux and FVLEG method with WENO5 reconstruction (from top to bottom) with  $N = 32$ . Contour lines are equally spaced from  $-1.1 \times 10^{-4} \text{ s}^{-1}$  to  $-1 \times 10^{-5} \text{ s}^{-1}$  in dashed lines and from  $1 \times 10^{-5} \text{ s}^{-1}$  to  $1.5 \times 10^{-4} \text{ s}^{-1}$  in solid lines with an interval of  $2 \times 10^{-5} \text{ s}^{-1}$ .

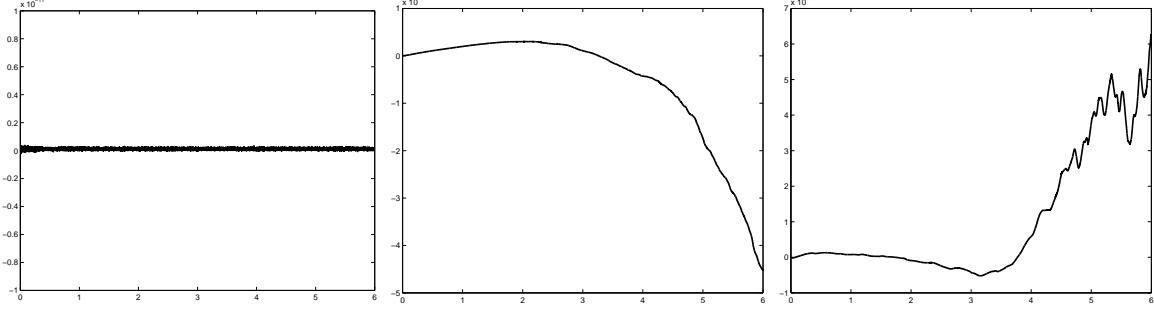


Fig. 4.20. Example 4.7: Same as Fig. 4.3 except for example 4.7 with  $N = 32$ .

#### A.1 The inner points on the cell edge within the subregion

Without loss of generality, consider the point  $(x_m^G, y_k, t_n)$ , denoted by  $P_0$ , on the bottom edge of cell  $C_{j+\frac{1}{2}, k+\frac{1}{2}}$ . Only the edge  $\mathcal{L}_{P_0} = \{(x, y_k) | x_{j-1} \leq x \leq x_j\}$  intersects with the closed curve  $\mathcal{C}_P^n = \{(x_j - d_1^{(\ell)}(\theta)\tau, y_k - d_2^{(\ell)}(\theta)\tau, t_n) = \mathbf{Q}(\theta) | \ell = 1, 3, \theta \in [0, 2\pi)\}$  possibly, under the restriction on  $\Delta t_n$  in (3.1). Obviously, the number of interaction points between the edge  $\mathcal{L}_{P_0}$  with the closed curve  $\mathcal{C}_P^n$  is equal to the number of real solutions to the algebraic equation  $d_2^{(1)}(\theta) = 0$ .

**Lemma A.1** *If the inequality*

$$|\tilde{v}| < \tilde{c}\sqrt{\tilde{g}^{22}\tilde{h}}, \quad (\text{A.1})$$

*holds, then  $d_2^{(1)}(\theta) = 0$  has two real solutions, which are located in the interval  $(-\frac{\pi}{2}, \frac{\pi}{2})$  and  $(\frac{\pi}{2}, \frac{3\pi}{2})$ , respectively; otherwise, it has less than two real solutions.*

**Proof** Since  $d_2^{(1)}(\theta)$  is a  $2\pi$ -periodic function of  $\theta$ , our attention may be restricted to the interval  $[-\frac{\pi}{2}, \frac{3\pi}{2}]$ . Taking the derivative of  $d_2^{(1)}(\theta)$  with respect to  $\theta$  gives

$$\frac{d}{d\theta}d_2^{(1)}(\theta) = -\frac{\tilde{c}}{\tilde{\Lambda}\tilde{K}_\theta^3}\cos\theta.$$

Because  $-\frac{\tilde{c}}{\tilde{\Lambda}\tilde{K}_\theta^3} < 0$ , the function  $d_2^{(1)}(\theta)$  decreases monotonically in the interval  $[-\frac{\pi}{2}, \frac{\pi}{2}]$  and increases monotonically in the interval  $[\frac{\pi}{2}, \frac{3\pi}{2}]$  so that the maximum and minimum values of  $d_2^{(1)}(\theta)$  are

$$\begin{aligned} \max_{\theta \in [-\frac{\pi}{2}, \frac{3\pi}{2}]} d_2^{(1)}(\theta) &= d_2^{(1)}(-\frac{\pi}{2}) = \tilde{v} + \tilde{c}\sqrt{\tilde{g}^{22}\tilde{h}}, \\ \min_{\theta \in [-\frac{\pi}{2}, \frac{3\pi}{2}]} d_2^{(1)}(\theta) &= d_2^{(1)}(\frac{\pi}{2}) = \tilde{v} - \tilde{c}\sqrt{\tilde{g}^{22}\tilde{h}}. \end{aligned}$$

Therefore, the sufficient and necessary condition for that  $d_2^{(1)}(\theta) = 0$  has two real solutions is

$$\min_{\theta \in [-\frac{\pi}{2}, \frac{3\pi}{2}]} d_2^{(1)}(\theta) < 0 < \max_{\theta \in [-\frac{\pi}{2}, \frac{3\pi}{2}]} d_2^{(1)}(\theta),$$

which is equivalent to (A.1). It completes the proof. ■



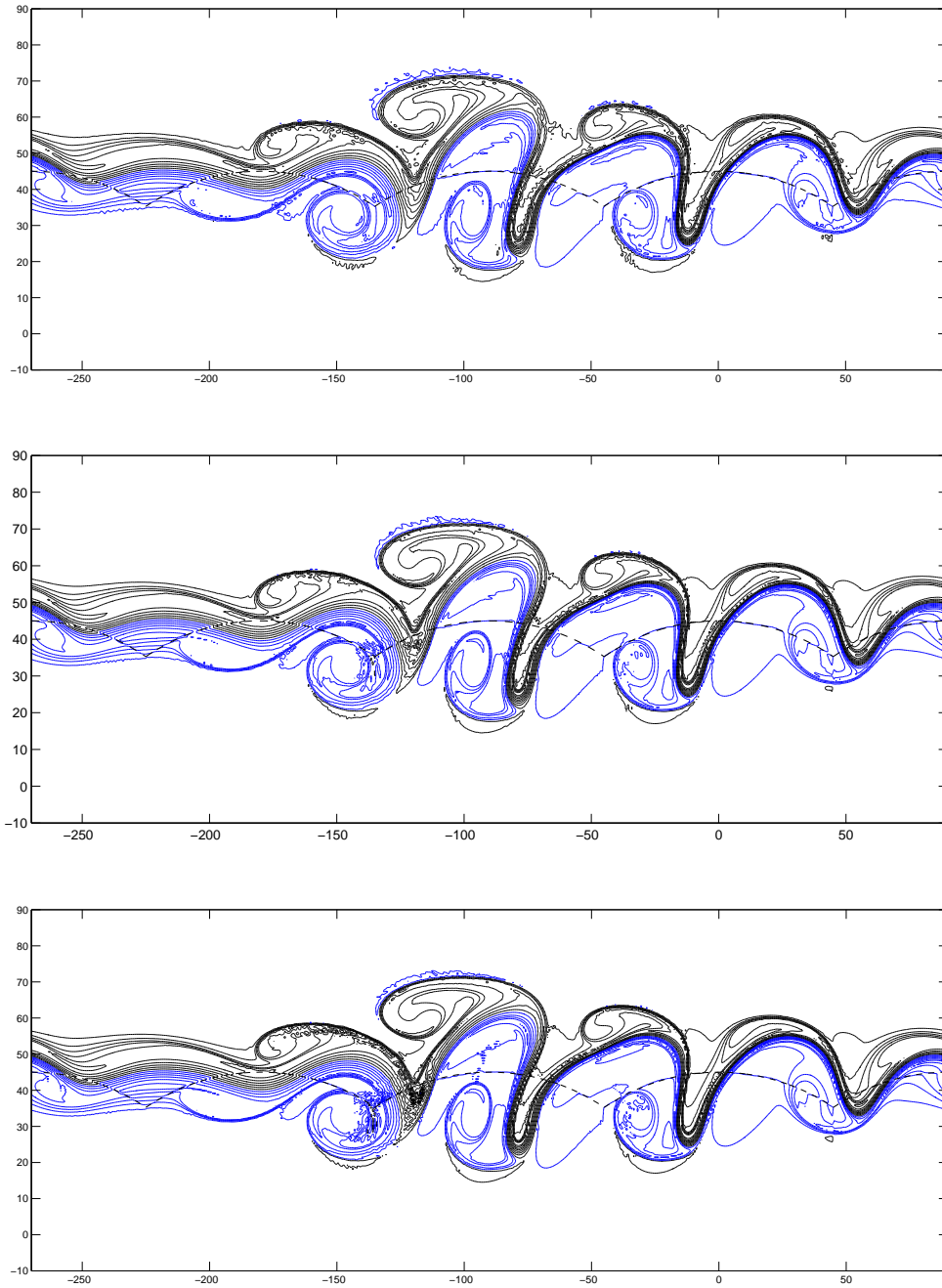


Fig. 4.21. Example 4.7: Relative vorticity obtained by using  $\mathbb{P}^3$ -based RKLEG method with  $N = 64, 96,$  and  $128$  (from top to bottom) at  $t = 6$  days.

With the aid of Lemma A.1,  $\theta_i$  may be evaluated as follows:

- If the inequality (A.1) holds, then the nonlinear equation  $d_2^{(1)}(\theta) = 0$  is iteratively

solved by using Newton's method

$$\theta^{(m+1)} = \theta^{(m)} - \frac{d_2^{(1)}(\theta^{(m)})}{\frac{d}{d\theta}d_2^{(1)}(\theta^{(m)})}, \quad m = 0, 1, 2, 3, \dots,$$

with the initial guesses  $\theta^{(0)} = 0$  and  $\pi$  respectively to get two approximate solutions  $\theta_1$  and  $\theta_2$ , and set  $\hat{N} = 2$  in the approximate evolution operator  $\mathcal{E}_h(\tau)$  or  $\mathcal{E}_{h,0}$ .

- If the inequality (A.1) does not hold, then set  $\hat{N} = 1$  and  $\theta_1 = 0$  in the approximate evolution operator  $\mathcal{E}_h(\tau)$  or  $\mathcal{E}_{h,0}$ .

### A.2 The end points on the cell edge within the subregion

Use  $P_0$  and  $P$  to denote the grid points  $(x_j, y_k, t_n)$  and  $(x_j, y_k, t_n + \tau)$  respectively, and consider the possible intersection points between the bicharacteristic cone past  $P$  and the four cell edges  $\mathcal{L}_{P_0}^\ell, \ell = 1, 2, 3, 4$ . The angles  $\theta_i$  corresponding to those intersection points may be evaluated by solving the equations  $d_1^{(1)}(\theta) = 0$  and  $d_2^{(1)}(\theta) = 0$ , respectively. Similarly, for the first equation, the following conclusion holds.

**Lemma A.2** *If the inequality*

$$|\tilde{u}| < \tilde{c}\sqrt{\tilde{g}^{11}\tilde{h}}, \quad (\text{A.2})$$

*holds, then the equation  $d_1^{(1)}(\theta) = 0$  has two real solutions, which are located in the interval  $(0, \pi)$  and  $(\pi, 2\pi)$ , respectively; otherwise, it has less than two real solutions.*

With the help of Lemmas A.1 and A.2, the value of  $\theta_i$  may be evaluated as follows:

- If both (A.1) and (A.2) do not hold, then set  $\hat{N} = 1, \theta_1 = 0$ .
- If (A.1) holds while (A.2) does not hold, then iteratively solve  $d_2^{(1)}(\theta) = 0$  with Newton's method to get its two solutions denoted by  $\theta_1$  and  $\theta_2$  with the initial guesses 0 and  $\pi$  respectively, and set  $\hat{N} = 2$ .
- If (A.2) holds while (A.1) does not hold, then iteratively solve  $d_1^{(1)}(\theta) = 0$  with Newton's method to get its two solutions denoted by  $\theta_1$  and  $\theta_2$  with the initial guesses  $\frac{\pi}{2}$  and  $\frac{3\pi}{2}$  respectively, and set  $\hat{N} = 2$ .
- If both (A.1) and (A.2) hold, then iteratively solve  $d_2^{(1)}(\theta) = 0$  and  $d_1^{(1)}(\theta) = 0$  with Newton's method to obtain four angles, which are labeled in anticlockwise direction as  $\theta_1, \theta_2, \theta_3, \theta_4$ , and set  $\hat{N} = 4$ .

## Appendix B

This appendix presents the detailed procedure to evaluate  $\{\theta_i, i = 1, 2, \dots, \hat{N}\}$  in the approximate evolution operator  $\mathcal{E}_h(\tau)$  or  $\mathcal{E}_{h,0}$  for the subregion boundaries in the LAT/LON



$(\xi, \eta)$  plane, see Section 3.3.3. For the sake of convenience, use  $\mathcal{L}_i$  to denote the subregion boundary between the  $i$ th and  $((i+1) \bmod 4)$ th subregions,  $i = 1, 2, 3, 4$ . Also use  $\mathcal{L}_i^{up}$  (resp.  $\mathcal{L}_i^{down}$ ) to denote the subregion boundary between  $i$ th and 5th (resp. 6th) subregions,  $i = 1, 2, 3, 4$ .

The subregion boundaries  $\mathcal{L}_1$  and  $\mathcal{L}_1^{up}$  are only discussed in the following, because other subregion boundaries may be similarly treated by using the translation and reflection transformations.

### B.1 The inner points of the cell edge on the subregion boundary

Since the cell edges  $\partial C_{j+\frac{1}{2}, k+\frac{1}{2}}$  on  $\mathcal{L}_1$  in the LAT/LON  $(\xi, \eta)$  plane are just part of the longitude lines (i.e.  $\xi = \text{const}$ ), the number of interaction points between the edge  $\mathcal{L}_1$  and the bottom of the bicharacteristic cone is equal to the number of real solutions to the algebraic equation  $d_2^{(1)}(\theta) = 0$  such that the method in Appendix A.1 may be directly used to evaluate the value of  $\theta_i$ .

The cell edge  $\partial C_{j+\frac{1}{2}, k+\frac{1}{2}}$  on  $\mathcal{L}_1^{up}$  in the LAT/LON  $(\xi, \eta)$  plane consists of those curves satisfying the equation

$$\tan \eta = \cos \xi \tan y, \quad (\text{B.1})$$

where  $y = y_{\hat{N}}$  and  $\xi \in [-\frac{\pi}{4}, \frac{\pi}{4}]$ . Use  $(\xi_0, \eta_0)$  to denote the inner point on the cell edges  $(x, y_N)$  in the LAT/LON  $(\xi, \eta)$  plane. The task is to get the intersection points between the curve (B.1) and

$$\mathcal{C}_P^n = \left\{ \left( x - d_1^{(\ell)}(\theta)\tau, y_N - d_2^{(\ell)}(\theta)\tau, t_n \right) = \mathbf{Q}(\theta) \mid \ell = 1, 3, \theta \in [0, 2\pi) \right\}.$$

Substituting point  $(\xi_0 - d_1^{(1)}(\theta)\tau, \eta_0 - d_2^{(1)}(\theta)\tau)$  into the equation (B.1) gives

$$\tan(\eta_0 - d_2^{(1)}(\theta)\tau) = \cos(\xi_0 - d_1^{(1)}(\theta)\tau) \tan y_N,$$

thus one has

$$\tan \eta_0 - \tan(\eta_0 - d_2^{(1)}(\theta)\tau) = \cos \xi_0 \tan y_N - \cos(\xi_0 - d_1^{(1)}(\theta)\tau) \tan y_N.$$

Using Lagrange's mean value theorem, and letting  $\tau \rightarrow 0$ , one yields

$$\sec^2 \eta_0 d_2^{(1)}(\theta) = -\sin \xi_0 d_1^{(1)}(\theta). \quad (\text{B.2})$$

**Lemma B.1** *If the inequality*

$$\mathcal{F}_c(\theta_{\min}, \xi_0, \eta_0, y_N) < 0 < \mathcal{F}_c(\theta_{\max}, \xi_0, \eta_0, y_N), \quad (\text{B.3})$$

*holds, where  $\mathcal{F}_c(\theta, \xi_0, \eta_0, y) := \sec^2 \eta_0 d_2^{(1)}(\theta) + \sin \xi_0 d_1^{(1)}(\theta) \tan y$ , then (B.2) has two real solutions, which are located in the interval  $(\theta_{\min}, \theta_{\max})$  and  $(\theta_{\max}, \theta_{\min} + 2\pi)$ , respectively;*

otherwise, it has less than two real solutions, where  $\theta_{\min}$  satisfies

$$\sin \xi_0 \sin \theta \tan y_N - \sec^2 \eta_0 \cos \theta = \sqrt{\sin^2 \xi_0 \tan^2 y_N + \sec^4 \eta_0 \sin(\theta - \theta_{\min})},$$

and  $\theta_{\max} = \theta_{\min} + \pi$ .

With the aid of Lemma B.1, the value of  $\theta_i$  may be evaluated as follows:

- If (B.3) holds, then iteratively solve  $\mathcal{F}_c(\theta, \xi_0, \eta_0, y_N) = 0$  with Newton's method to get its two solutions denoted by  $\theta_1$  and  $\theta_2$  with the initial guesses  $\frac{1}{2}(\theta_{\min} + \theta_{\max})$  and  $\frac{1}{2}(\theta_{\min} + \theta_{\max}) + \pi$ , respectively, and set  $\hat{N} = 2$ .
- If (B.3) does not hold, then set  $\hat{N} = 1$ ,  $\theta_1 = 0$ .

### B.2 The end points of the cell edge on the subregion boundary

Use  $P_0$ , and  $P$  to denote the grid points  $(x_N, y_k, t_n)$  and  $(x_N, y_k, t_n + \tau)$  on  $\mathcal{L}_1$ . In this case, the cell edges on  $\mathcal{L}_1$  mapping to the LAT/LON  $(\xi, \eta)$  plane are part of the longitude lines (i.e.  $\xi = \text{const}$ ), and the curves satisfying (B.1) and  $\tan \eta = \cos(\xi - \frac{\pi}{2}) \tan y$  respectively, where  $y = y_k$ , see schematic diagram in Fig B.1 (a). Use  $(\xi_0, \eta_0)$  to denote the LAT/LON coordinates of the end points of the cell edges  $(x_N, y_k)$ . Corresponding angles  $\theta_i$  of two possible intersection points between the edge (i.e.  $\xi = \text{const}$ ) and the bottom of the bicharacteristic cone may be evaluated by solving  $d_1^{(1)}(\theta) = 0$ , while the angles  $\theta_i$  corresponding to other interaction points are gotten by solving the following equations

$$\begin{cases} \mathcal{F}_c(\theta, \xi_0, \eta_0, y_k) = 0, & d_1^{(1)}(\theta) > 0, \\ \mathcal{F}_c(\theta, \xi_0 - \frac{\pi}{2}, \eta_0, y_k) = 0, & d_1^{(1)}(\theta) < 0. \end{cases}$$

Using the procedure in Appendix A.2 gives  $\hat{N}$  and  $\theta_i, i = 1, \dots, \hat{N}$ .

The cell edges on  $\mathcal{L}_1^{up}$  mapping to the LAT/LON plane are the longitude line (i.e.  $\xi = \text{const}$ ), or the curve satisfying (B.1) or  $\tan \xi \tan x = \sin \lambda$ , here  $x = x_j, y = y_N, \xi \in [-\frac{\pi}{4}, \frac{\pi}{4}]$ , and  $(\xi, \eta)$  denotes the point on the cell edges in the LAT/LON plane, see schematic diagram in Fig B.1 (b). Use  $(\xi_0, \eta_0)$  to denote the end point of the cell edges  $(x_j, y_N)$  in the LAT/LON space. The angles relating to the intersection points between the cell edges and the bottom of the bicharacteristic cone may be obtained by solving the equation  $\mathcal{F}_c(\theta, \xi_0, \eta_0, y_N) = 0$ , and

$$\begin{cases} d_2^{(1)}(\theta) = 0, & \mathcal{F}_c(\theta, \xi_0, \eta_0, y_N) > 0, \\ \mathcal{F}_s(\theta, \xi_0, \eta_0, x_j) = 0, & \mathcal{F}_c(\theta, \xi_0, \eta_0, y_N) < 0, \end{cases}$$

respectively, where

$$\mathcal{F}_s(\theta, \xi_0, \eta_0, x_j) := \sec^2 \eta_0 \tan x_j d_2^{(1)}(\theta) - \cos \xi_0 d_1^{(1)}(\theta). \quad (\text{B.4})$$

For the equation  $\mathcal{F}_s(\theta, \xi_0, \eta_0, x_j) = 0$ , the following conclusion holds.

**Lemma B.2** *If the inequality*

$$\mathcal{F}_s(\theta_{\min}, \xi_0, \eta_0, x_j) < 0 < \mathcal{F}_s(\theta_{\max}, \xi_0, \eta_0, x_j), \quad (\text{B.5})$$

*holds, then the equation  $\mathcal{F}_s(\theta, \xi_0, \eta_0, x_j) = 0$  has two real solutions, which are in the interval  $(\theta_{\min}, \theta_{\max})$  and  $(\theta_{\max}, \theta_{\min} + 2\pi)$ , respectively; otherwise, it has less than two real solutions, where  $\theta_{\min}$  satisfies*

$$-\sec^2 \eta_0 \tan x_j \cos \theta - \cos \xi_0 \sin \theta = \sqrt{\sec^4 \eta_0 \tan^2 x_j + \cos^2 \xi_0 \sin(\theta - \theta_{\min})},$$

and  $\theta_{\max} = \theta_{\min} + \pi$ .

It means that two solutions of the equation  $\mathcal{F}_s(\theta, \xi_0, \eta_0, x_j) = 0$  may be iteratively gotten by using Newton's method with the initial guesses  $\frac{1}{2}(\theta_{\min} + \theta_{\max})$  and  $\frac{1}{2}(\theta_{\min} + \theta_{\max}) + \pi$ , respectively, if (B.5) holds.

Following the procedure in Appendix A.2 gives  $\hat{N}$  and  $\theta_i, i = 1, \dots, \hat{N}$ .

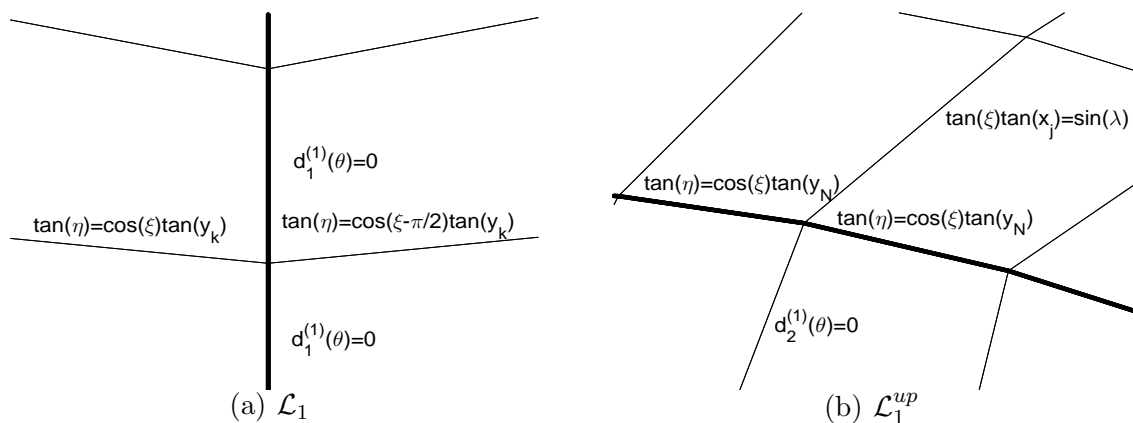


Fig. B.1. Schematic diagram of the subregion boundary.

## References

- [1] K.R. Arun, M. Kraft, M. Lukáčová-Medvid'ová, and P. Prasad, Finite volume evolution Galerkin method for hyperbolic conservation laws with spatially varying flux functions, *J. Comput. Phys.*, 228 (2009), 565-590.
- [2] J.R. Bates, F.H.M. Semazzi, and R.W. Higgins, Integration of the shallow water equations on the sphere using a vector semi-Lagrangian scheme with a multigrid solver, *Mon. Wea. Rev.*, 118 (1990), 1615-1627.
- [3] B.J. Block, M. Lukáčová-Medvid'ová, P. Virnau, and L.Yelash, Accelerated GPU simulation of compressible flow by the discontinuous evolution Galerkin method, *Eur. Phys. J. -Spec. Top.*, 210 (2012), 119-132.

- [4] A. Bollermann, S. Noelle, and M. Lukáčová-Medvid'ová, Finite volume evolution Galerkin methods for the shallow water equations with dry beds, *Commun. Comput. Phys.*, 10 (2011), 371-404.
- [5] D.S. Butler, The numerical solution of hyperbolic systems of partial differential equations in three independent variables, *Proc. R. Soc. Lond. A.*, 255 (1960), 232-252.
- [6] C.G. Chen, X.L. Li, X.S. Shen, and F. Xiao, Global shallow water models based on multi-moment constrained finite volume method and three quasi-uniform spherical grids, *J. Comput. Phys.*, 271 (2014), 191-223.
- [7] C.G. Chen and F. Xiao, Shallow water model on cubed-sphere by multi-moment finite volume method, *J. Comput. Phys.*, 227 (2008), 5019-5044.
- [8] B. Cockburn and C.-W. Shu, The Runge-Kutta discontinuous Galerkin method for conservation laws V: multidimensional systems, *J. Comput. Phys.*, 141 (1998), 199-224.
- [9] M. Dudzinski and M. Lukáčová-Medvid'ová, Well-balanced bicharacteristic-based scheme for multilayer shallow water flows including wet/dry fronts, *J. Comput. Phys.* 235 (2013), 82-113.
- [10] J. Galewsky, R.K. Scott, and L.M. Polvani, An initial-value problem for testing numerical models of the global shallow-water equations, *Tellus A*, 56 (2004), 429-440.
- [11] F.X. Giraldo, J.S. Hesthaven, and T. Warburton, Nodal high-order discontinuous Galerkin methods for the shallow water equations, *J. Comput. Phys.*, 181 (2002), 499-525.
- [12] F.X. Giraldo and T. Warburton, A nodal triangle-based spectral element method for the shallow water equations on the sphere, *J. Comput. Phys.*, 207 (2005), 129-150.
- [13] F.X. Giraldo and T. Warburton, A high-order triangular discontinuous Galerkin oceanic shallow water model, *Int. J. Numer. Meth. Fluids.*, 56 (2008), 899-925.
- [14] L.C. Huang, Conservative bicharacteristic upwind schemes for hyperbolic conservation laws II, *Comput. Math. Appl.*, 29 (1995), 91-107.
- [15] A. Hundertmark-Zaušková, M. Lukáčová-Medvid'ová, and F. Prill, Large time step finite volume evolution Galerkin methods, *J. Sci. Comput.* 48 (2011), 227-240.
- [16] R. Jakob-Chien, J.J. Hack, and D.L. Williamson, Spectral transform solutions to the shallow water test set, *J. Comput. Phys.*, 119 (1995), 164-187.
- [17] R.L. Johnston and S.K. Pal, The numerical solution of hyperbolic systems using bicharacteristics, *Math. Comp.*, 26 (1972), 377-392.
- [18] A. Kageyama and T. Sato, The "Yin-Yang grid": An overset grid in spherical geometry, *Geochem. Geophys. Geosyst.*, 5 (2004), Q09005.
- [19] M. Läuter, F.X. Giraldo, D. Handorf, and K. Dethloff, A discontinuous Galerkin method for the shallow water equations in spherical triangular coordinates, *J. Comput. Phys.*, 227 (2008), 10226-10242.
- [20] M. Läuter, D. Handorf, and K. Dethloff, Unsteady analytical solutions of the spherical shallow water equations, *J. Comput. Phys.*, 210 (2005), 535-553.

- [21] J.L. Lee and A.E. MacDonald, A finite-volume icosahedral shallow-water model on a local coordinates, *Mon. Wea. Rev.*, 137 (2009), 1422-1437.
- [22] X.L. Li, D.H. Chen, X.D. Peng, K. Takahashi, and F. Xiao, A multimoment finite volume shallow-water model on the Yin-Yang overset spherical grid, *Mon. Wea. Rev.*, 136 (2008), 3066-3086.
- [23] X.L. Li, X.S. Shen, X.D. Peng, F. Xiao, Z.R. Zhuang, and C.G. Chen, Fourth order transport model on Yin-Yang grid by multi-moment constrained finite volume scheme, *Proc. Comput. Sci.*, 9 (2012), 1004-1013.
- [24] S.J. Lin and R.B. Rood, An explicit flux-form semi-Lagrangian shallow-water model on the sphere, *Quart. J. Roy. Meteor. Soc.*, 123 (1997), 2477-2498.
- [25] M. Lukáčová-Medvid'ová and K.W. Morton, Finite volume evolution Galerkin methods—A survey, *Indian J. Pure & Appl. Math.*, 41 (2010), 329-361.
- [26] M. Lukáčová-Medvid'ová, K.W. Morton, and G. Warnecke, Finite volume evolution Galerkin methods for Euler equations of gas dynamics, *Int. J. Numer. Meth. Fluids.*, 40 (2002), 425-434.
- [27] M. Lukáčová-Medvid'ová, K.W. Morton, and G. Warnecke, Evolution Galerkin methods for hyperbolic systems in two space dimensions, *Math. Comput.*, 69 (2000), 1355-1384.
- [28] M. Lukáčová-Medvid'ová, K.W. Morton, and G. Warnecke, Finite volume evolution Galerkin (FVEG) methods for hyperbolic problems, *SIAM. J. Sci. Comput.*, 26 (2004), 1-30.
- [29] M. Lukáčová-Medvid'ová, S. Noelle, and M. Kraft, Well-balanced finite volume evolution Galerkin methods for the shallow water problems, *J. Comput. Phys.*, 221 (2007), 122-147.
- [30] M. Lukáčová-Medvid'ová, J. Saibertová, and G. Warnecke, Finite volume evolution Galerkin methods for nonlinear hyperbolic systems, *J. Comput. Phys.*, 183 (2002), 533-562.
- [31] A. McDonald and J.R. Bates, Semi-Lagrangian integration of a gridpoint shallow water model on the sphere, *Mon. Wea. Rev.*, 117 (1989), 130-137.
- [32] K.W. Morton, On the analysis of finite volume methods for evolutionary problems, *SIAM J. Numer. Anal.*, 35 (1998), 2195-2222.
- [33] R.D. Nair and B. Machenhauer, The mass-conservative cell-integrated semi-Lagrangian advection scheme on the sphere, *Mon. Wea. Rev.*, 130 (2002), 649-667.
- [34] R.D. Nair, S.J. Thomas, and R.D. Loft, A discontinuous Galerkin transport scheme on the cubed sphere, *Mon. Wea. Rev.*, 133 (2005), 814-828.
- [35] R.D. Nair, S.J. Thomas, and R.D. Loft, A discontinuous Galerkin global shallow water model, *Mon. Wea. Rev.*, 133 (2005), 876-888.
- [36] J.A. Pudykiewicz, On numerical solution of the shallow water equations with chemical reactions on icosahedral geodesic grid, *J. Comput. Phys.*, 230 (2011), 1956-1991.
- [37] W.M. Putman and S.J. Lin, Finite-volume transport on various cubed-sphere grid, *J. Comput. Phys.*, 227 (2007), 55-78.

- [38] C. Ronchi, R. Iacono, and P.S. Paolucci, The “cubed sphere”: A new method for the solution of partial differential equations in spherical geometry, *J. Comput. Phys.*, 124 (1996), 93-114.
- [39] R. Sadourny, Conservative finite-difference approximations of the primitive equations on quasi-uniform spherical grids, *Mon. Wea. Rev.*, 100 (1972), 136-144.
- [40] C.-W. Shu, Total-variation-diminishing time discretizations, *SIAM J. Sci & Stat. Comput.*, 9 (1988), 1073-1084.
- [41] A. St-Cyr, C. Jablonowski, J.M. Dennis, H.M. Tufo, and S.J. Thomas, A comparison of two shallow-water models with non-conforming adaptive grids, *Mon. Wea. Rev.*, 136 (2008), 1898-1922.
- [42] Y.T. Sun and Y.X. Ren, The finite volume local evolution Galerkin method for solving the hyperbolic conservation laws, *J. Comput. Phys.*, 228 (2009), 4945-4960.
- [43] M. Taylor, J. Tribbia, and M. Iskandarani, The spectral element method for the shallow water equations on the sphere, *J. Comput. Phys.*, 130 (1997), 92-108.
- [44] S.J. Thomas and R. D. Loft, Semi-implicit spectral element model, *J. Sci. Comput.*, 17(2002), 339-350.
- [45] S.J. Thomas and R.D. Loft, The NCAR spectral element climate dynamical core: semi-implicit Eulerian formulation, *J. Sci. Comput.*, 25 (2005), 307-322.
- [46] J. Thuburn, A PV-based shallow-water model on a hexagonal-icosahedral grid, *Mon. Wea. Rev.*, 125 (1997), 2328-2347.
- [47] H. Tomita, M. Tsugawa, M. Satoh, and K. Goto, Shallow-water model on a modified icosahedral geodesic grid by using spring dynamics, *J. Comput. Phys.*, 174 (2001), 579-613.
- [48] P.A. Ullrich, C. Jablonowski, and B. van Leer, High-order finite-volume methods for the shallow water equations on the sphere, *J. Comput. Phys.*, 229 (2010), 6104-6134.
- [49] D.L. Williamson, J.B. Drake J.J. Hack, R. Jakob, and P.N. Swarztrauber, A standard test set for numerical approximations to the shallow water equations in spherical geometry, *J. Comput. Phys.*, 102 (1992), 211-224.
- [50] K.L. Wu and H.Z. Tang, Finite volume local evolution Galerkin method for two-dimensional special relativistic hydrodynamics, *J. Comput. Phys.*, 256 (2014), 277-307.
- [51] C. Yang, J.W. Cao, and X.C. Cai, A fully implicit domain decomposition algorithm for shallow water equations on the cubed-sphere, *SIAM J. Sci. Comput.*, 32 (2010), 418-438.
- [52] L. Yelash, A. Müller, M. Lukáčová-Medvid’ová, F.X. Giraldo, and S.V. Wirth, Adaptive discontinuous evolution Galerkin method for dry atmospheric flow, *J. Comput. Phys.*, 268 (2014), 106-133.
- [53] J. Zhao and H.Z. Tang, Runge-Kutta discontinuous Galerkin methods with WENO limiter for the special relativistic hydrodynamics, *J. Comput. Phys.*, 242 (2013), 138-168.